ACS APPLIED MATERIALS & INTERFACES

www.acsami.org Research Article

Efficient Purification of Ethylene from C_2 Hydrocarbons with an C_2H_6/C_2H_2-Selective Metal–Organic Framework

Shan-Qing Yang,[#] Fang-Zhou Sun,[#] Puxu Liu, Libo Li, Rajamani Krishna, Ying-Hui Zhang, Quanwen Li, Lei Zhou, and Tong-Liang Hu*

Cite This: *ACS Appl. Mater. Interfaces* 2021, 13, 962–969 Read Online

ACCESS | Metrics & More | Article Recommendations | Supporting Information

ABSTRACT: The separation of ethylene (C_2H_4) from C_2 hydrocarbons is considered as one of the most difficult and important processes in the petrochemical industry. Heat-driven cryogenic distillation is still widely used in the C_2 hydrocarbons separation realms, which is an energy intensive process and takes up immense space. In response to a greener, more energy-efficient sustainable development, we successfully synthesized a multifunction microporous Mg-based MOF $[Mg_2(TCPE)(\mu_2\text{-}OH_2)(DMA)_2]$·solvents (**NUM-9**) with C_2H_6/C_2H_2 selectivity based on a physical adsorption mechanism, and with outstanding stability; especially, it is stable up to 500 °C under an air atmosphere. **NUM-9a** (activated **NUM-9**) shows good performances in the separation of C_2H_6/C_2H_2 from raw ethylene gases. In addition, its actual separation potential is also examined by IAST and dynamic column breakthrough experiments. GCMC calculation results indicate that the unique structure of **NUM-9a** is primarily conducive to the selective adsorption of C_2H_6 and C_2H_2. More importantly, compared with C_2H_4, **NUM-9a** prefers to selectively adsorb C_2H_6 and C_2H_2 simultaneously, which makes **NUM-9a** as a sorbent have the capacity to separate C_2H_4 from C_2 hydrocarbon mixtures under mild conditions through a greener and energy-efficient separation strategy.

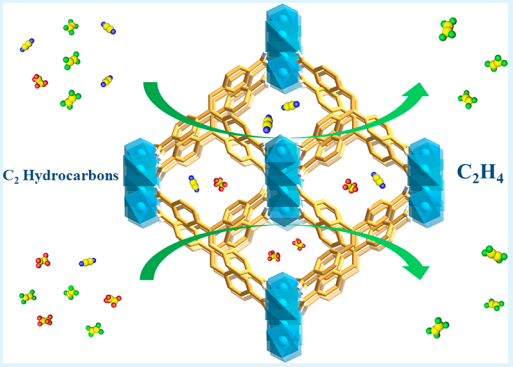

KEYWORDS: *Mg metal–organic framework, high thermal stability, separation of C_2 hydrocarbons, C_2H_6/C_2H_2 selectivity, purification of ethylene*

INTRODUCTION

Ethylene (C_2H_4) is indispensable in the petrochemical industry and widely used to produce polyethylene, ethylene oxide, and so on, in which the annual global production is hundreds of million tons,[1] as called industrial blood.[2] There are many methods for the production of C_2H_4 in the petrochemical industry, such as steam cracking with naphtha and catalytic cracking of light hydrocarbons. The production of C_2H_4 based on steam cracking of naphtha occupies a large proportion in the petrochemical industry and is still the main method of producing C_2H_4 up to date, in which the process ineluctably leads into a small amount of C_2H_6 and C_2H_2 as impurities, which does not meet C_2H_4 purity requirements. The existence of C_2H_6 extends reactor residence time and reduces production per unit time; what's more, C_2H_6 often leaves the process of polymerization with the emission of gases, posing a potential hazard to human health and safety. The presence of C_2H_2 in C_2H_4 raw material will be toxic to the catalysts used in the polymerization process and then notably have a bad impact on the production quality of polyethylene. Moreover, C_2H_2 reacts with metal catalysts/pipeline to form solid metal acetylides, which can block the fluid and result in explosion. Therefore, the impurities of C_2H_6 and C_2H_2 should be purified and the concentration should be reduced to meet the requirements. However, because of their similar physical properties, including very similar molecule size (C_2H_2: 3.32 × 3.34 × 5.70 Å^3, C_2H_4: 3.28 × 4.18 × 4.84 Å^3, C_2H_6: 4.08 × 3.81 × 4.82 Å^3)[3,4] and volatility, the separation of C_2H_4 from C_2 hydrocarbons is considered as one of the most difficult and important processes.[1] Heat-driven cryogenic distillation is still widely used to separate these mixture substances, which is an energy intensive process and takes up immense space.[5,6] In response to a greener, more energy-efficient development, more efforts have been devoted to develop an efficient separation strategy, especially based on a physical adsorption mechanism. Adsorption separation using the porous solid materials is an alternative, such as zeolite, activated carbon, and γ-Al_2O_3.[7−9] These conventional materials face problems of this kind or that kind. On the one hand, there is poor selectivity owing to the scarcity of specific recognition of molecular

Received: November 9, 2020
Accepted: December 14, 2020
Published: December 28, 2020

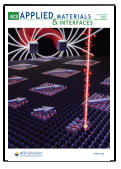

https://dx.doi.org/10.1021/acsami.0c20000
ACS Appl. Mater. Interfaces 2021, 13, 962–969

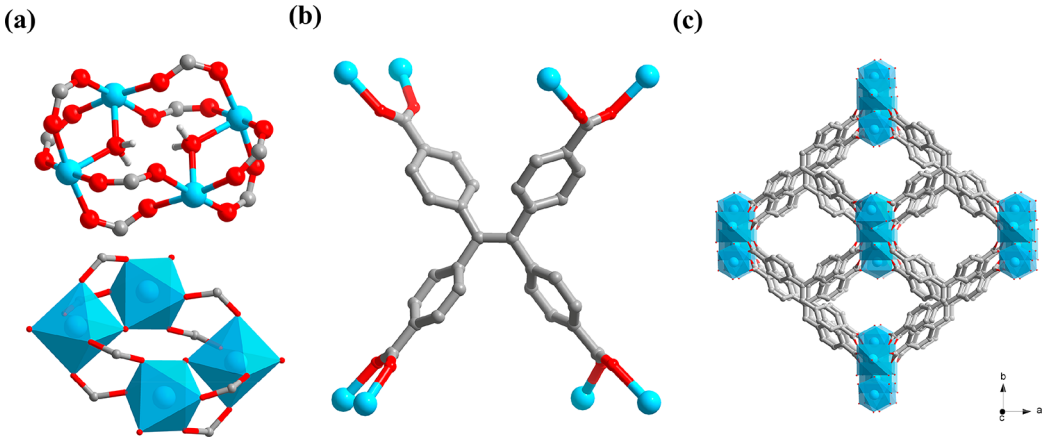

Figure 1. (a) The tetranuclear magnesium(II) cluster in the crystal structure of **NUM-9** (Mg: sky blue; C: dark gray; O: red). (b) The coordination form of the entire $TCPE^{4-}$ ligand. (c) The three-dimensional framework exhibits one-dimensional diamond channels from the *c* axis. Hydrogen atoms and solvent molecules were omitted for clarity.

properties; on the other hand, the adsorption capacity of these conventional materials is also limited.[10]

In recent years, as one kind of emerging porous material, metal−organic frameworks (MOFs), also known as porous coordination polymers (PCPs), which consist of metal or metal clusters nodes and ligand linkers exhibit more typical characteristics, such as designable pore sizes and multifunctional surface, that make them show broad application prospects in the realms of gas adsorption and separation, such as C_2H_4/C_2H_6,[11−13] C_2H_2/C_2H_4,[14,15] C_3H_6/C_3H_8,[16−18] and CO_2/C_2H_2.[19,20] So far, a succession of advances have been made through making use of MOFs as adsorbents in the field of binary separation[19−33] and a few ternary separations.[34−37]

However, the use of MOFs as adsorbents in the separation of C_2 hydrocarbons is suffering from either poor selectivity because of their similar molecule sizes or low uptake amounts due to smaller pore volume. Furthermore, for the C_2H_6/C_2H_4 binary mixture separation, it is easier to adsorb ethylene owing to the formation of π-complexation between the unsaturated metal ions and the double bond with ethylene like other conventional materials, so that it still needs a desorption process that increases the energy consumption, and it also brings challenges to the separation and purification of C_2H_4. For the C_2H_2/C_2H_4 mixture, the adsorbents generally have stronger binding affinity with C_2H_2 due to the difference of polarizability, which facilitates direct purification of C_2H_4. Considering that the amounts of C_2H_6 and C_2H_2 occupy relatively small percentages in the C_2H_4 raw material, so as long as C_2H_6 and C_2H_2 are preferentially adsorbed, it may be possible to achieve the separation of C_2H_4 from C_2 hydrocarbons directly. Nevertheless, to date, the MOFs which act as multifunction adsorbents preferring to simultaneously adsorb C_2H_6 and C_2H_2 to achieve purification of ethylene are still very rare.[34,36]

Herein, we have exploited such a microporous MOF $[Mg_2(TCPE)(\mu_2\text{-}OH_2)(DMA)_2]$·solvents (**NUM-9**, H_4TCPE = 4,4′,4″,4‴-(ethene-1,1,2,2-tetrayl) tetrabenzoic acid, DMA = *N*,*N*-dimethylacetamide) based on a physical adsorption mechanism with excellent thermal and solvent stabilities for efficient separation of C_2H_4 from C_2 hydrocarbons. Gas adsorption isotherms indicate that **NUM-9a** preferentially adsorbs C_2H_6 and C_2H_2 from C_2 hydrocarbon mixtures, and the heat of adsorption also verifies this view. The practical separation potential has been established by IAST selectivities calculations and the breakthrough experiments, and the binding affinity sites for C_2 hydrocarbons have been evidenced by Grand Canonical Monte Carlo (GCMC) calculations. All the results show that **NUM-9a** has multi-functions, and it can realize the efficient separation of C_2H_4 from C_2 hydrocarbon mixtures so that the purpose of saving energy and green development is achieved.

EXPERIMENTAL SECTION

Materials and Method. All the chemical reagents and solvents were received from commercial suppliers in high purity and used without further purification. Thermogravimetric analyses (TGA) were performed on a Rigaku standard TG-DTA analyzer from room temperature to 800 °C under an air atmosphere with a heating rate of 10 °C min^{-1}, using an empty and clean Al_2O_3 crucible as reference. Powder X-ray diffraction (PXRD) patterns were collected on a Rigaku Miniflex 600 at 40 kV and 15 mA with a scan rate of 5.0 deg min^{-1}, using Cu−Kα radiation in an air atmosphere. In situ variable temperature PXRD (VT-PXRD) patterns were collected on a Bruker D8 diffractometer.

Synthesis of NUM-9 ($[Mg_2(TCPE)(\mu_2\text{-}OH_2)(DMA)_2]$·Solvents). A mixture of $Mg(NO_3)_2{\cdot}4H_2O$ (20 mg, 0.1 mmol), H_4TCPE (10 mg, 0.01 mmol, H_4TCPE = 4,4′,4″,4‴-(ethene-1,1,2,2-tetrayl) tetrabenzoic acid) was dissolved with DMA (1.5 mL), CH_3CH_2OH (1 mL), and deionized water (0.3 mL) in a 10 mL screw-capped glass vial, and then the sealed vial was heated to 100 °C for 72 h, which was then cooled to room temperature. The light yellow near rectangular block crystals obtained were washed several times with DMA for single-crystal X-ray diffraction analysis. Yield: 89% based on H_4TCPE.

Activation of NUM-9 (NUM-9a). The fresh sample of **NUM-9** was guest exchanged with anhydrous acetone five times, and the solvent-exchange sample was evacuated less than 10^{-5} Torr at 150 °C for 10 h to obtain the **NUM-9a**.

Single-Component Gas Adsorption Measurements. The single-component gas adsorption/desorption isotherms of N_2, C_2H_6, C_2H_4, and C_2H_2 were measured at different temperatures (77 K for N_2; 273, 298, and 313 K for C_2H_6, C_2H_4, and C_2H_2). The N_2 adsorption isotherm for pressures within 0−1.0 bar was measured at 77 K with liquid nitrogen using a Micrometrics ASAP 2460 volumetric gas adsorption analyzer. A sample of **NUM-9a** (about 100 mg) was used for the sorption measurement of C_2 hydrocarbons from 273 to 313 K, which was precisely controlled with a LAUDR RP890 recirculating control system containing dry ethanol by a Micrometrics ASAP 2020M volumetric gas adsorption analyzer.

Dynamic Breakthrough Experiment. In the column breakthrough experiment, 0.9040 g of adsorbent (**NUM-9**) was packed into

https://dx.doi.org/10.1021/acsami.0c20000
ACS Appl. Mater. Interfaces 2021, 13, 962−969

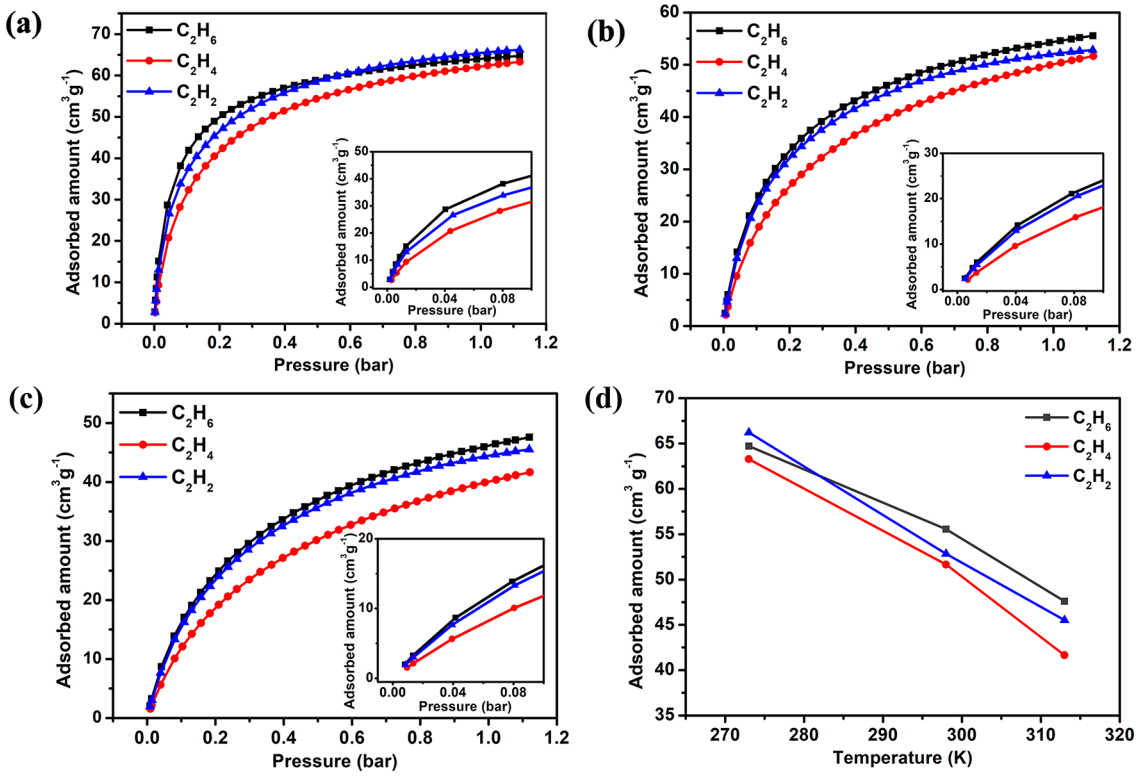

Figure 2. Single-component gas adsorption isotherms for C_2H_6 (dark gray), C_2H_4 (red), and C_2H_2 (blue) of **NUM-9a** at (a) 273 K, (b) 298 K, and (c) 313 K. (d) Tendency of adsorbed amounts of C_2H_6, C_2H_4, and C_2H_2 with the change of temperature.

a customized quartz column (4 mm inner diameter × 100 mm) with quartz wool padding the void space. **NUM-9** was in-site activated at 423 K under vacuum to obtain the purity adsorbent and then was purged with He flow at 2 mL min^{-1}. The gas mixtures of C_2H_6/C_2H_4 and C_2H_2/C_2H_4 flow were also leaded into at 2 mL min^{-1}, and the outlet concentration was monitored with gas chromatography (TCD-Thermal Conductivity Detector, detection limit 0.1%).

RESULTS AND DISCUSSION

Single-crystal X-ray diffraction revealed that **NUM-9** crystallizes in the orthorhombic system with *Cmca* space group. The asymmetric unit of **NUM-9** contains two crystallographically independent Mg^{2+}, half of a $TCPE^{4-}$ ligand, one bridged water (μ_2-OH_2), and two coordinated DMA molecules. Two types of Mg^{2+} exhibit a 6-coordination model, and they are both coordinated with four oxygen atoms from different carboxylate groups of $TCPE^{4-}$, one oxygen atom from a DMA molecule, and one bridged oxygen atom of μ_2-OH_2. The two Mg^{2+} ions are connected by two carboxyl groups and one bridged oxygen atom of μ_2-OH_2, and two pairs of Mg^{2+} are linked to each other by four shared carboxyl groups (Figure 1a), forming a tetranuclear magnesium(II) cluster. There are two DMA molecules per pair of two magnesium(II) ions, so the tetranuclear magnesium(II) cluster can be identified as an 8-connected node linked by eight $TCPE^{4-}$ ligands. Furthermore, the Mg^{2+} clusters are connected to $TCPE^{4-}$ ligands to form a three-dimensional framework with zigzag-shaped square channels, generating one-dimensional approximately square channels with the pore size about 4.5 × 4.5 $Å^2$ along the *c* axis (Figure 1c). On the basis of the single-crystal X-ray diffraction data, the experimental PXRD pattern of the synthesized **NUM-9** is consistent well with the simulated pattern, indicating that the synthesized bulk **NUM-9** has high phase purity (Figure S1).

Then we explored the stability of **NUM-9**. The results of VT-PXRD show that the MOF has excellent thermal property sustained to 500 °C (Figure S2). The thermogravimetric curve was carried out under a flowing air atmosphere; as shown in Figure S3, it can be seen that **NUM-9** can maintain stability up to approximately 500 °C, which is completely consistent with the result of VT-PXRD. The structure of **NUM-9** has slightly changed at about 190 °C and eventually collapsed at 500 °C. Furthermore, we tested the solvent stability of **NUM-9** in different solvents (Figures S4 and S5), and this material also exhibits excellent performance. In addition, the crystal characteristic of **NUM-9** can still be maintained after the sample activation, which was confirmed by matching its PXRD pattern with the pattern of the as-synthesized sample (Figure S6). Obviously, **NUM-9** shows high thermal and solvent stability, which stimulated us to explore the adsorption and separation performance of this material.

To investigate the gas adsorption capacity, the first is to confirm the permanent porosity of the material. We prepared the activated **NUM-9a** by high vacuum at 423 K with the acetone-exchanged sample; then the permanent porosity of **NUM-9a** was verified by the N_2 sorption isotherm at 77 K. As shown in Figure S7, a completely reversible type I isotherm apparently indicates the microporous nature of **NUM-9a**. The Brunauer–Emmett–Teller (Langmuir) surface area based on the nitrogen adsorption isotherm is about 330 $m^2 g^{-1}$ (371 $m^2 g^{-1}$) for **NUM-9a**. The pore size distribution of **NUM-9a** exported from the nitrogen adsorption isotherm in the light of the Horvath–Kawazoe method shows a pore approximately at 3.6 Å (Figure S8), which is a little lower than that measured from the single crystal structure, owing to the slightly deficient

https://dx.doi.org/10.1021/acsami.0c20000
ACS Appl. Mater. Interfaces 2021, 13, 962–969

filling of N_2 on the fluctuant pore surfaces. It may have some application in gas adsorption and separation inspired by its structure, which is abundant with benzene rings, and may have strong interactions with adsorbed gases. On the basis of the above analysis, we try to explore the adsorption and separation potential of this compound toward C_2 hydrocarbons. The single-component equilibrium adsorption isotherms for C_2H_6, C_2H_4, and C_2H_2 were measured first at different temperatures (273, 298, and 313 K). All adsorption isotherms are completely reversible, and the adsorption curves are only shown for the purpose of clarity in Figure 2a–c. Not surprisingly, the uptake amounts of adsorbed gases show a downward trend with the temperature increasing (Figure 2d). The exciting part is that **NUM-9a** can adsorb higher C_2H_6 and C_2H_2 than C_2H_4 in all the analysis conditions, which implies a C_2H_6/C_2H_2-selective performance in **NUM-9a**. Moreover, as the temperature increases, the difference in the uptake capacity of the adsorbed gases becomes obvious. The uptake of the adsorbed gases is relatively close at 1.0 bar and 273 K (C_2H_6: 64.05 $cm^3\ g^{-1}$, C_2H_4: 62.22 $cm^3\ g^{-1}$, C_2H_2: 65.52 $cm^3\ g^{-1}$; uptake capacity difference ratio is 3% and 5% for C_2H_6/C_2H_4 and C_2H_2/C_2H_4, respectively), and the difference of uptake amount is conspicuous at 313 K and 1.0 bar (C_2H_6: 46.19 $cm^3\ g^{-1}$, C_2H_4: 40.04 $cm^3\ g^{-1}$, C_2H_2: 44.46 $cm^3\ g^{-1}$; uptake capacity difference ratio is 13% and 11% for C_2H_6/C_2H_4 and C_2H_2/C_2H_4, respectively). The uptake amount of C_2H_6 is about 55.55 $cm^3\ g^{-1}$ (2.48 mmol g^{-1}) at 298 K and 1.0 bar, higher than that of many famous MOFs, such as ZIF-7 (1.85 mmol g^{-1})[38] and MAF-49 (1.73 mmol g^{-1}),[11] and lower than that of some excellent MOFs, such as $Fe_2(O)_2(dobdc)$ (3.32 mmol g^{-1}),[39] TJT-100 (3.84 mmol g^{-1}),[34] MUF-15 (4.69 mmol g^{-1}),[21] and JNU-2 (4.19 mmol g^{-1}).[35] Furthermore, observing the gas adsorption curves, it can also be seen that there may also be better separation performance between C_2H_4 and C_2H_2. The obvious difference of adsorption capacity and the characteristic of selective adsorption may achieve the separation of C_2H_4 from C_2 hydrocarbons. Generally, gas adsorption selectivity is associated with adsorption performance in the low-pressure area; then we carefully evaluate the adsorption performance of each gas in the low-pressure area at 273, 298, and 313 K. Near the low-pressure area, the adsorption isotherms of C_2H_6 and C_2H_2 are steeper than that of C_2H_4, indicating the interaction of adsorbents and the framework is stronger; at the same time, we can conclude that **NUM-9a** has multifunction performance in the separation realms of C_2H_6/C_2H_4 and C_2H_2/C_2H_4, in which **NUM-9a** may possess the characteristic of achieving the one-step purification of C_2H_4 from C_2 hydrocarbons.

In order to quantitatively illustrate the binding affinity of **NUM-9a** toward C_2H_6, C_2H_4, and C_2H_2, the coverage dependent adsorption enthalpies (Q_{st}) of **NUM-9a** for C_2H_6, C_2H_4, and C_2H_2 were evaluated experimentally from single-component isotherms collected at 273, 298, and 313 K based on the method of a virial equation. As shown in Figure 3, the collected Q_{st} values at zero coverage are 35.75, 32.32, and 35.79 kJ mol^{-1} for C_2H_6, C_2H_4, and C_2H_2, respectively. The Q_{st} values for C_2H_6 and C_2H_2 are somewhat higher than that for C_2H_4 at zero coverage, which indicates **NUM-9** has the relatively stronger affinity for C_2H_6 and C_2H_2 than C_2H_4 with an abnormal phenomenon. Moreover, the calculation result of Q_{st} is consistent with the experimental results.

To comprehend the preferential adsorption behavior of C_2H_6 and C_2H_2 than C_2H_4, we carried out GCMC simulation

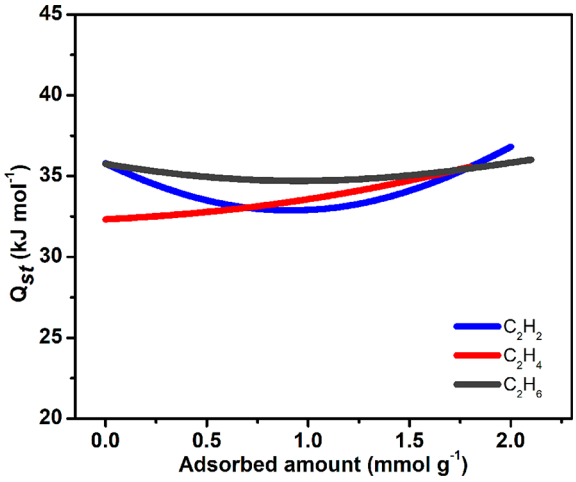

Figure 3. Isosteric enthalpy of adsorption (Q_{st}) of C_2H_6, C_2H_4, and C_2H_2 for **NUM-9a** evaluated by the method of a virial equation fits at 298 and 313 K.

to calculate the energy distribution of C_2 hydrocarbons in **NUM-9a** at 313 K and 1.0 bar. Primarily C–H···O and C–H···π interactions and open metal sites could be found after loading of C_2 hydrocarbon molecules into the skeleton of **NUM-9a**. As shown in Figure 4, the largest C_2H_6 molecule and the most complex spatial configuration in C_2 hydrocarbons make it have more interactions with the framework, and it can interact with the framework by forming four C–H···O (H···O 3.399(0)–3.516(3) Å). At the same time, more hydrogens are forming multi C–H···π (C–H···π 2.905(8)–4.027(2) Å) interactions between an C_2H_6 molecule and the phenyl rings within the channels. Owing to the existence of open metal sites, both C_2H_2 and C_2H_4 may interact with the coordination unsaturated metal ions. However, due to the larger distance of open metal sites and the C_2H_4 molecule, the interaction could be ignored. The plane configuration of the C_2H_4 molecule interacts with the framework through three C–H···O (H···O 2.787(0)–3.497(7) Å) and two C–H···π (C–H···π 3.537(3)–3.542(5) Å), so the interactions between C_2H_4 and the framework mainly depend on the C–H···O and C–H···π. The linear C_2H_2 molecule with a triple bond has a strong interaction with the coordination unsaturated Mg^{2+} provided by removing the oxygen atom of the DMA molecule (C≡C··· Mg 2.796(5)–2.936(3) Å). Moreover, C_2H_2 molecules interact with the framework through four C–H···O (H···O 3.004(9)–3.491(8) Å). So the C_2H_2 molecules show the strongest interactions with the framework, and then the largest C_2H_6 molecules form the more C–H···O and C–H···π interactions than that for C_2H_4. Overall, the calculation results showed the stronger host-guest interactions for C_2H_2 and C_2H_6 rather than that of C_2H_4. In addition, the energy distribution of C_2H_2 was wider compared with that of C_2H_6 and C_2H_4, which indicated two kinds of preferential adsorption sites for C_2H_2 (Figure S24). Obviously, the results of energy distribution for C_2 hydrocarbons were consistent with the trend of adsorption isotherms. The reason for such an adsorption behavior of C_2 hydrocarbons can be ascribed to the difference in the interactions of C–H···O and C–H···π between subject and guests; moreover, the coordination unsaturated metal ions played an important role in these adsorption behaviors.

https://dx.doi.org/10.1021/acsami.0c20000
ACS Appl. Mater. Interfaces 2021, 13, 962–969

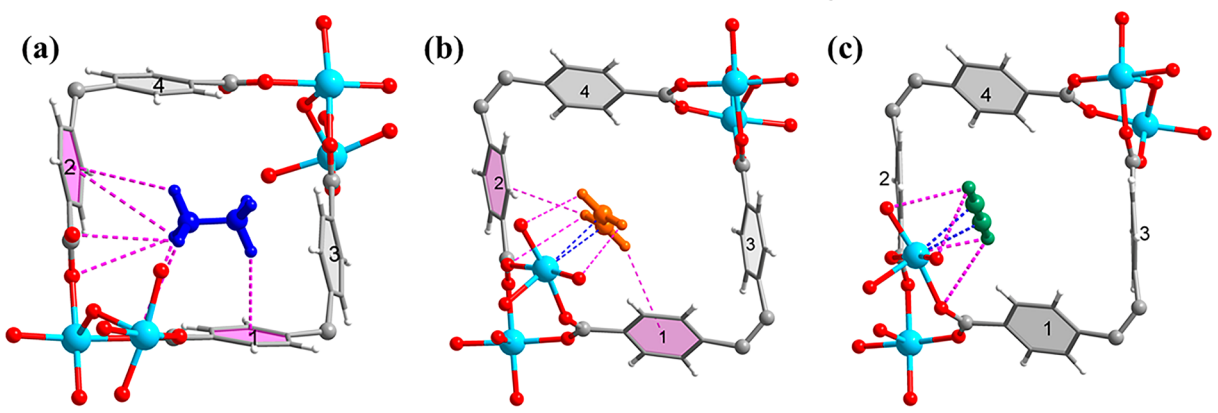

Figure 4. Results of GCMC simulations, exhibiting the adsorption sites for (a) C_2H_6, (b) C_2H_4, and (c) C_2H_2 in **NUM-9a**. The sequence number of benzene rings is determined by the distance between the benzene ring and the hydrogen atoms on the guest molecule. (The C−H···π and C−H···O interactions are highlighted in pink dashed bonds, and the interactions between unsaturated bonds and open metal sites are highlighted in blue dashed bonds. The displayed distance of C−H···O is within 3.5 Å, and the distance between gray benzene and the nearest guest molecules is over 4.0 Å.)

NUM-9a has a series of typical characteristics of the high adsorption capacities and strong binding affinity for C_2H_6 and C_2H_2; therefore, it has the potential excellent property of purifying C_2H_4 from the mixtures of C_2H_6/C_2H_4 and C_2H_2/C_2H_4. So we further evaluated these adsorption selectivities of C_2H_6/C_2H_4 (10/90) and C_2H_2/C_2H_4 (1/99) for **NUM-9a** using ideal adsorbed solution theory (IAST). As shown in Figure 5, the adsorption selectivity of C_2H_6/C_2H_4 at 100 kPa

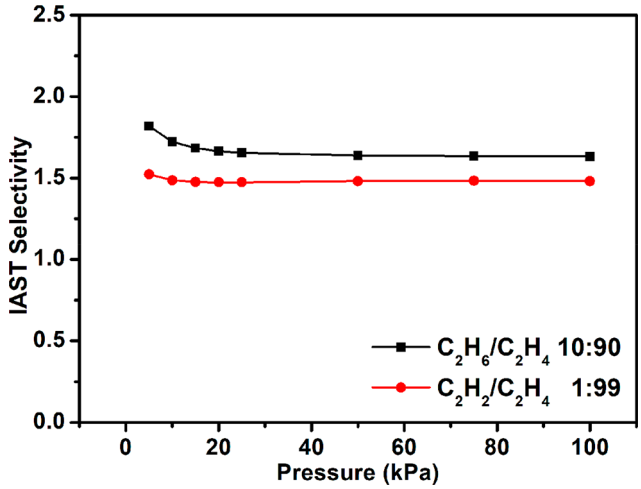

Figure 5. IAST selectivities of mixtures of C_2H_6/C_2H_4 (10/90, v/v) and C_2H_2/C_2H_4 (1/99, v/v) for **NUM-9a** at 313 K.

and 298 K is determined to around 1.62 and can reach 1.63 at 100 kPa and 313 K, and the value is around 1.48 for C_2H_2/C_2H_4 at 298 and 313 K. By the calculation of IAST, operating the experiment at 313 K is a better condition, in which the adsorption selectivity values of both C_2H_6/C_2H_4 and C_2H_2/C_2H_4 can reach approximately 1.5. The adsorption selectivity of C_2H_6/C_2H_4 (50/50) also was calculated considering that the most of the C_2H_6-selective MOFs' calculated C_2H_6/C_2H_4 binary mixture ratio is 50:50. As shown in Figure S29, the adsorption selectivity of C_2H_6/C_2H_4 (50/50) at 100 kPa and 298 K is determined to around 1.61. This value is also higher than that of many famous MOFs reported, such as ZIF-7 (1.5),[38] MIL-142A (1.51),[40] UTSA-33 (1.4),[41] UTSA-35 (1.4),[42] and ZIU-121a (1.51),[43] but lower than that of partial top-performing MOFs, such as $Fe_2(O_2)$(dobdc) (4.4)[39] and ZJU-120a (2.74).[43]

To further examine the C_2H_6/C_2H_4 and C_2H_2/C_2H_4 practical separation performance of **NUM-9a**, breakthrough experiments were carried out where the C_2H_6/C_2H_4 mixture concentration ratio of 10/90 (v/v) and the C_2H_2/C_2H_4 mixture concentration ratio of 1/99 (v/v) were injected into a packed column of **NUM-9a** with a rate of 2 mL min^{-1} at 313 K. As shown in Figure 6a,b, the results of breakthrough experiments show that the **NUM-9a** is a multifunction material, which can preferentially detect C_2H_4 in the C_2H_6/C_2H_4 and C_2H_2/C_2H_4 breakthrough experiment to achieve the purpose of C_2H_4 purification without more desorption. In terms of total flow and breakthrough time, compared with other C_2H_6-selective MOFs, such as PCN-245,[10] PCN-250,[44] and MIL-142A,[40] **NUM-9a**'s performance is quite good. And **NUM-9a** exhibited the separation ability for the C_2H_6/C_2H_4 binary mixture comparable to some materials, such as ZJU-120a.[43] **NUM-9a** not only can selectively adsorb C_2H_6 but also showed the excellent separation performance for the C_2H_2/C_2H_4 mixture. Obviously, C_2H_6/C_2H_2-selective MOFs can achieve efficient separation in that C_2H_4 is obtained directly and simplifies the separation procedure.

Accordingly, **NUM-9a** exhibits not only an C_2H_6/C_2H_2-selective behavior but also the outstanding C_2H_6/C_2H_4 and C_2H_2/C_2H_4 binary mixture separation performances. In light of the unique adsorption behavior, the $C_2H_6/C_2H_4/C_2H_2$ (9/90/1, v/v/v) ternary mixture, close to an actual separation process, the separation performance with **NUM-9a** has been evaluated by transient breakthrough simulations, which can be used as a guide for actual industrial implementation potential. As shown in Figure 6c,d, indeed, **NUM-9a** shows a certain performance of $C_2H_6/C_2H_4/C_2H_2$ mixture separation, which indicates the adsorbent possesses the capacity of one-step purification of C_2H_4.

CONCLUSIONS

In summary, we report a multifunction microporous Mg-based MOF (**NUM-9**) with prominent structure stability. The good IAST selectivity values and favorable dynamic column breakthrough experiments exhibit that **NUM-9** selectively

https://dx.doi.org/10.1021/acsami.0c20000
ACS Appl. Mater. Interfaces 2021, 13, 962−969

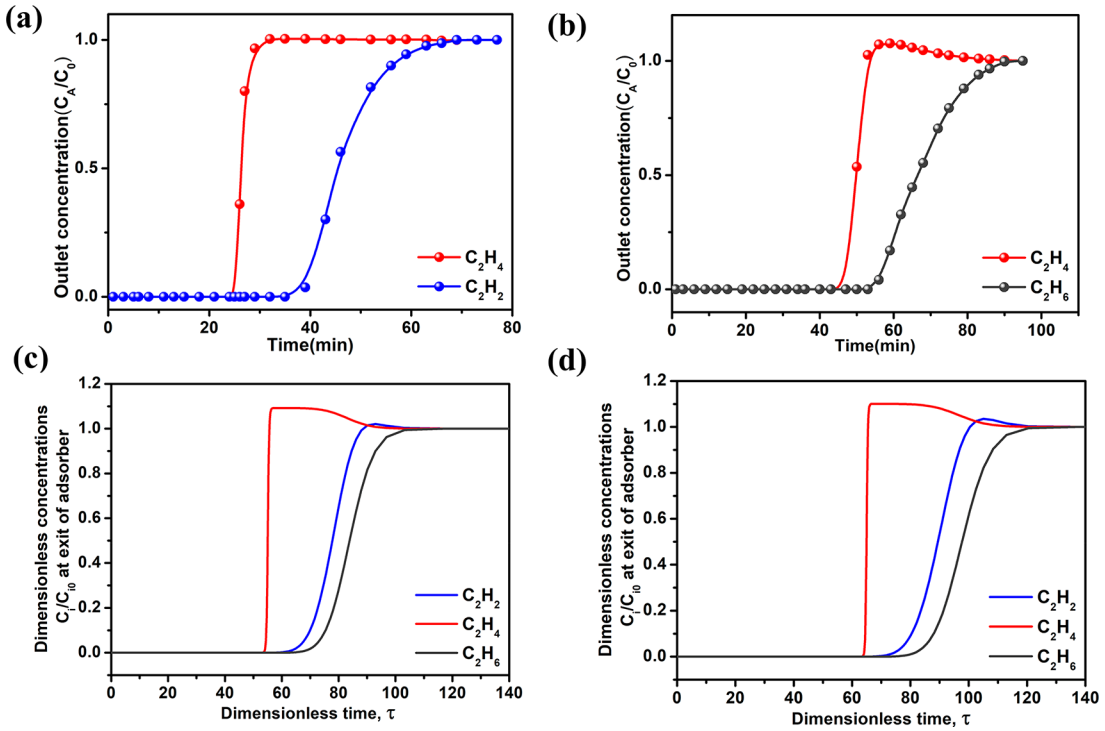

Figure 6. Dynamic breakthrough curves for mixture gases of (a) C_2H_6/C_2H_4 (10/90, v/v) and (b) C_2H_2/C_2H_4 (1/99, v/v). The experiments were carried out at a total pressure of 1.0 bar and 313 K. (c, d) Transient breakthrough curves of $C_2H_2/C_2H_4/C_2H_6$ (1/90/10, v/v/v) ternary mixture in an adsorber bed packed using **NUM-9a**. Two different operating temperatures were 298 K (c) and 313 K (d). The total bulk gas phase in the fixed bed is 100 kPa and 313 K.

adsorbs C_2H_6 and C_2H_2, showing the characteristic of C_2H_6/C_2H_2 selectivity. Due to the interaction difference between the subject and guest, **NUM-9a** possesses properties of purifying C_2H_4 from C_2 hydrocarbons, which show excellent performances in the separation of C_2H_6/C_2H_4, C_2H_2/C_2H_4, and C_2/C_2H_4. This work will promote the goal of one-step purification of ethylene, which can meet the requirements of green and energy-efficient sustainable society development. Furthermore, the research will promote the application of MOFs in the separation realms, and more efforts should be given to achieve the greener process of separation and purification.

■ ASSOCIATED CONTENT

Supporting Information

The Supporting Information is available free of charge at https://pubs.acs.org/doi/10.1021/acsami.0c20000.

Full experimental details, including crystal data, crystal structure, PXRD patterns, TGA curves, N_2 sorption data, and Grand Canonical Monte Carlo (GCMC) simulations (PDF)

Crystallographic data of **NUM-9** (CIF)

■ AUTHOR INFORMATION

Corresponding Author

Tong-Liang Hu − *School of Materials Science and Engineering, Tianjin Key Laboratory of Metal and Molecule-Based Material Chemistry, National Institute for Advanced Materials and Tianjin Key Lab for Rare Earth Materials and Applications, Nankai University, Tianjin 300350, China; State Key Laboratory of Coordination Chemistry, Nanjing University, Nanjing 210023, China;* orcid.org/0000-0001-9619-9867; Email: tlhu@nankai.edu.cn

Authors

Shan-Qing Yang − *School of Materials Science and Engineering, Tianjin Key Laboratory of Metal and Molecule-Based Material Chemistry, National Institute for Advanced Materials, Nankai University, Tianjin 300350, China*

Fang-Zhou Sun − *School of Materials Science and Engineering, Tianjin Key Laboratory of Metal and Molecule-Based Material Chemistry, National Institute for Advanced Materials, Nankai University, Tianjin 300350, China*

Puxu Liu − *College of Chemistry and Chemical Engineering, Shanxi Key Laboratory of Gas Energy Efficient and Clean Utilization, Taiyuan University of Technology, Taiyuan 030024, Shanxi, China*

Libo Li − *College of Chemistry and Chemical Engineering, Shanxi Key Laboratory of Gas Energy Efficient and Clean Utilization, Taiyuan University of Technology, Taiyuan 030024, Shanxi, China;* orcid.org/0000-0001-7147-9838

Rajamani Krishna − *Van 't Hoff Institute for Molecular Sciences, University of Amsterdam, 1098 XH Amsterdam, The Netherlands;* orcid.org/0000-0002-4784-8530

Ying-Hui Zhang − *School of Materials Science and Engineering, Tianjin Key Laboratory of Metal and Molecule-Based Material Chemistry, National Institute for Advanced Materials, Nankai University, Tianjin 300350, China*

Quanwen Li − *School of Materials Science and Engineering, Tianjin Key Laboratory of Metal and Molecule-Based Material Chemistry, National Institute for Advanced Materials, Nankai University, Tianjin 300350, China*

Lei Zhou − *School of Materials Science and Engineering, Tianjin Key Laboratory of Metal and Molecule-Based Material Chemistry, National Institute for Advanced Materials, Nankai University, Tianjin 300350, China*

https://dx.doi.org/10.1021/acsami.0c20000
ACS Appl. Mater. Interfaces 2021, 13, 962−969

Complete contact information is available at:
https://pubs.acs.org/10.1021/acsami.0c20000

Author Contributions

#These authors contributed equally to this work.

Notes

The authors declare no competing financial interest.

■ ACKNOWLEDGMENTS

This work was financially supported by the National Natural Science Foundation of China (21673120 and 21922810), the Natural Science Foundation of Tianjin (20JCYBJC01330), and the Fundamental Research Funds for the Central Universities, Nankai University (63196005).

■ REFERENCES

(1) Sholl, D. S.; Lively, R. P. Seven Chemical Separations to Change the World. *Nature* **2016**, *532*, 435−437.
(2) Amghizar, I.; Vandewalle, L. A.; Van Geem, K. M.; Marin, G. B. New Trends in Olefin Production. *Engineering* **2017**, *3*, 171−178.
(3) Reid, C. R.; Thomas, K. M. Adsorption Kinetics and Size Exclusion Properties of Probe Molecules for the Selective Porosity in a Carbon Molecular Sieve Used for Air Separation. *J. Phys. Chem. B* **2001**, *105*, 10619−10629.
(4) Webster, C. E.; Drago, R. S.; Zerner, M. C. Molecular Dimensions for Adsorptives. *J. Am. Chem. Soc.* **1998**, *120*, 5509−5516.
(5) Li, J.-R.; Kuppler, R. J.; Zhou, H.-C Selective Gas Adsorption and Separation in Metal−Organic Frameworks. *Chem. Soc. Rev.* **2009**, *38*, 1477−1504.
(6) Li, B.; Zhang, Y.; Krishna, R.; Yao, K.; Han, Y.; Wu, Z.; Ma, D.; Shi, Z.; Pham, T.; Space, B.; Liu, J.; Thallapally, P. K.; Liu, J.; Chrzanowski, M.; Ma, S. Introduction of π-Complexation into Porous Aromatic Framework for Highly Selective Adsorption of Ethylene over Ethane. *J. Am. Chem. Soc.* **2014**, *136*, 8654−8660.
(7) Bereciartua, P. J.; Cantin, A.; Corma, A.; Jorda, J. L.; Palomino, M.; Rey, F.; Valencia, S.; Corcoran, E. W.; Kortunov, P.; Ravikovitch, P. I.; Burton, A.; Yoon, C.; Wang, Y.; Paur, C.; Guzman, J.; Bishop, A. R.; Casty, G. L. Control of Zeolite Framework Flexibility and Pore Topology for Separation of Ethane and Ethylene. *Science* **2017**, *358*, 1068−1071.
(8) Choi, B.-U.; Choi, D.-K.; Lee, Y.-W.; Lee, B.-K.; Kim, S.-H. Adsorption Equilibria of Methane, Ethane, Ethylene, Nitrogen, and Hydrogen onto Activated Carbon. *J. Chem. Eng. Data* **2003**, *48*, 603−607.
(9) Yang, R. T.; Kikkinides, E. S. New Sorbents for Olefin/Paraffin Separations by Adsorption via π-Complexation. *AIChE J.* **1995**, *41*, 509−517.
(10) Lv, D.; Shi, R.; Chen, Y.; Wu, Y.; Wu, H.; Xi, H.; Xia, Q.; Li, Z. Selective Adsorption of Ethane over Ethylene in PCN-245: Impacts of Interpenetrated Adsorbent. *ACS Appl. Mater. Interfaces* **2018**, *10*, 8366−8373.
(11) Liao, P.-Q.; Zhang, W.-X.; Zhang, J.-P.; Chen, X.-M Efficient Purification of Ethene by an Ethane-Trapping Metal-Organic Framework. *Nat. Commun.* **2015**, *6*, 8697.
(12) Cui, W.-G.; Hu, T.-L.; Bu, X.-H. Metal-Organic Framework Materials for the Separation and Purification of Light Hydrocarbons. *Adv. Mater.* **2020**, *32*, 1806445.
(13) Bao, Z.; Wang, J.; Zhang, Z.; Xing, H.; Yang, Q.; Yang, Y.; Wu, H.; Krishna, R.; Zhou, W.; Chen, B.; Ren, Q. Molecular Sieving of Ethane from Ethylene through the Molecular Cross-Section Size Differentiation in Gallate-based Metal−Organic Frameworks. *Angew. Chem., Int. Ed.* **2018**, *57*, 16020−16025.
(14) Wang, J.; Li, L.; Guo, L.; Zhao, Y.; Xie, D.; Zhang, Z.; Yang, Q.; Yang, Y.; Bao, Z.; Ren, Q. Adsorptive Separation of Acetylene from Ethylene in Isostructural Gallate-Based Metal−Organic Frameworks. *Chem. - Eur. J.* **2019**, *25*, 15516−15524.
(15) Peng, Y.-L.; Pham, T.; Li, P.; Wang, T.; Chen, Y.; Chen, K.-J.; Forrest, K. A.; Space, B.; Cheng, P.; Zaworotko, M. J.; Zhang, Z. Robust Ultramicroporous Metal-Organic Frameworks with Benchmark Affinity for Acetylene. *Angew. Chem., Int. Ed.* **2018**, *57*, 10971−109752.
(16) Geier, S. J.; Mason, J. A.; Bloch, E. D.; Queen, W. L.; Hudson, M. R.; Brown, C. M.; Long, J. R. Selective Adsorption of Ethylene over Ethane and Propylene over Propane in the etMal−Organic Frameworks M_2(dobdc) (M = Mg, Mn, Fe, Co, Ni, Zn). *Chem. Sci.* **2013**, *4*, 2054−2061.
(17) Wang, H.; Dong, X.; Colombo, V.; Wang, Q.; Liu, Y.; Liu, W.; Wang, X.-L.; Huang, X.-Y.; Proserpio, D. M.; Sironi, A.; Han, Y.; Li, J. Tailor-Made Microporous Metal-Organic Frameworks for the Full Separation of Propane from Propylene Through Selective Size Exclusion. *Adv. Mater.* **2018**, *30*, 1805088.
(18) Wang, Y.; Huang, N.-Y.; Zhang, X.-W.; He, H.; Huang, R.-K.; Ye, Z.-M.; Li, Y.; Zhou, D.-D.; Liao, P.-Q.; Chen, X.-M.; Zhang, J.-P Selective Aerobic Oxidation of Metal-Organic Framework Boosts Thermodynamic and Kinetic Propylene/Propane Selectivity. *Angew. Chem., Int. Ed.* **2019**, *58*, 7692−7696.
(19) Foo, M. L.; Matsuda, R.; Hijikata, Y.; Krishna, R.; Sato, H.; Horike, S.; Hori, A.; Duan, J.; Sato, Y.; Kubota, Y.; Takata, M.; Kitagawa, S. An Adsorbate Discriminatory Gate Effect in a Flexible Porous Coordination Polymer for Selective Adsorption of CO_2 over C_2H_2. *J. Am. Chem. Soc.* **2016**, *138*, 3022−3030.
(20) Moreau, F.; da Silva, I.; Al Smail, N. H.; Easun, T. L.; Savage, M.; Godfrey, H. G.; Parker, S. F.; Manuel, P.; Yang, S.; Schröder, M. Unravelling Exceptional Acetylene and Carbon Dioxide Adsorption within a Tetra-amide Functionalized Metal-Organic Framework. *Nat. Commun.* **2017**, *8*, 14085.
(21) Qazvini, O. T.; Babarao, R.; Shi, Z.-L.; Zhang, Y.-B.; Telfer, S. G. A Robust Ethane-Trapping Metal−Organic Framework with a High Capacity for Ethylene Purification. *J. Am. Chem. Soc.* **2019**, *141*, 5014−5020.
(22) Fan, W.; Wang, X.; Zhang, X.; Liu, X.; Wang, Y.; Kang, Z.; Dai, F.; Xu, B.; Wang, R.; Sun, D. Fine-Tuning the Pore Environment of the Microporous Cu-MOF for High Propylene Storage and Efficient Separation of Light Hydrocarbons. *ACS Cent. Sci.* **2019**, *5*, 1261−1268.
(23) Xu, M.-M.; Kong, X.-J.; He, T.; Wu, X.-Q.; Xie, L.-H.; Li, J.-R. Reaction Duration-Dependent Formation of Two Cu (II)-MOFs with Selective Adsorption Properties of C_3H_4 over C_3H_6. *Dalton Trans.* **2019**, *48*, 9225−9233.
(24) Zeng, H.; Xie, M.; Huang, Y.-L.; Zhao, Y.; Xie, X.-J.; Bai, J.-P.; Wan, M.-Y.; Krishna, R.; Lu, W.; Li, D. Induced Fit of C_2H_2 in a Flexible MOF through Cooperative Action of Open Metal Sites. *Angew. Chem., Int. Ed.* **2019**, *58*, 8515−8519.
(25) Li, N.; Chang, Z.; Huang, H.; Feng, R.; He, W.-W.; Zhong, M.; Madden, D. G.; Zaworotko, M. J.; Bu, X.-H. Specific K^+ Binding Sites as CO_2 Traps in a Porous MOF for Enhanced CO_2 Selective Sorption. *Small* **2019**, *15*, 1900426.
(26) Yu, M.-H.; Space, B.; Franz, D.; Zhou, W.; He, C.; Li, L.; Krishna, R.; Chang, Z.; Li, W.; Hu, T.-L.; Bu, X.-H. Enhanced Gas Uptake in a Microporous Metal-Organic Framework via a Sorbate Induced-Fit Mechanism. *J. Am. Chem. Soc.* **2019**, *141*, 17703−17712.
(27) Sun, F.-Z.; Yang, S.-Q.; Krishna, R.; Zhang, Y.-H.; Xia, Y.-P.; Hu, T.-L. Microporous Metal−Organic Framework with a Completely Reversed Adsorption Relationship for C_2 Hydrocarbons at Room Temperature. *ACS Appl. Mater. Interfaces* **2020**, *12*, 6105−6111.
(28) Ding, M.; Flaig, R. W.; Jiang, H.-L.; Yaghi, O. M. Carbon Capture and Conversion Using Metal-Organic Frameworks and MOF-Based Materials. *Chem. Soc. Rev.* **2019**, *48*, 2783−2828.
(29) Li, L.; Guo, L.; Zhang, Z.; Yang, Q.; Yang, Y.; Bao, Z.; Ren, Q.; Li, J. A Robust Squarate-Based Metal-Organic Framework Demonstrates Record High Affinity and Selectivity for Xenon over Krypton. *J. Am. Chem. Soc.* **2019**, *141*, 9358−9364.
(30) Ma, D.-Y.; Li, Z.; Zhu, J.; Zhou, Y.; Chen, L.; Mai, X.; Liufu, M.; Wu, Y.; Li, Y. Inverse and highly selective separation of CO_2/

C_2H_2 on a thulium-organic framework. *J. Mater. Chem. A* **2020**, *8*, 11933−11937.
(31) Wu, K.; Guo, L.; Zhang, Z.; Yang, Q.; Yang, Y.; Ren, Q.; Bao, Z. Shaping of gallate-based metal-organic frameworks for adsorption separation of ethylene from acetylene and ethane. *J. Colloid Interface Sci.* **2021**, *581*, 177−184.
(32) Li, J.; Han, X.; Zhang, X.; Sheveleva, A. M.; Cheng, Y.; Tuna, F.; McInnes, E. J. L.; McCormick McPherson, L. J.; Teat, S. J.; Daemen, L. L.; Ramirez-Cuesta, A. J.; Schröder, M.; Yang, S. Capture of Nitrogen Dioxide and Conversion to Nitric Acid in a Porous Metal−Organic Framework. *Nat. Chem.* **2019**, *11*, 1085−1090.
(33) Zhai, Q. G.; Bu, X.; Mao, C.; Zhao, X.; Daemen, L.; Cheng, Y.; Ramirez-Cuesta, A. J.; Feng, P. An Ultra-Tunable Platform for Molecular Engineering of High-Performance Crystalline Porous Materials. *Nat. Commun.* **2016**, *7*, 13645.
(34) Hao, H.-G.; Zhao, Y.-F.; Chen, D.-M.; Yu, J.-M.; Tan, K.; Ma, S.; Chabal, Y.; Zhang, Z.-M.; Dou, J.-M.; Xiao, Z.-H.; Day, G.; Zhou, H.-C.; Lu, T.-B. Simultaneous Trapping of C_2H_2 and C_2H_6 from a Ternary Mixture of $C_2H_2/C_2H_4/C_2H_6$ in a Robust Metal-Organic Framework for the Purification of C_2H_4. *Angew. Chem., Int. Ed.* **2018**, *57*, 16067−16071.
(35) Zeng, H.; Xie, X. J.; Xie, M.; Huang, Y. L.; Luo, D.; Wang, T.; Zhao, Y.; Lu, W.; Li, D. A. Cage-Interconnected Metal-Organic Framework with Tailored Apertures for Efficient C_2H_6/C_2H_4 Separation under Humid Conditions. *J. Am. Chem. Soc.* **2019**, *141*, 20390−20396.
(36) Xu, Z.; Xiong, X.; Xiong, J.; Krishna, R.; Li, L.; Fan, Y.; Luo, F.; Chen, B. A Robust Th-azole Framework for Highly Efficient Purification of C_2H_4 from a $C_2H_4/C_2H_2/C_2H_6$ Mixture. *Nat. Commun.* **2020**, *11*, 3163.
(37) Dong, Q.; Zhang, X.; Liu, S.; Lin, R.-B.; Guo, Y.; Ma, Y.; Yonezu, A.; Krishna, R.; Liu, G.; Duan, J.; Matsuda, R.; Jin, W.; Chen, B. Tuning Gate-Opening of a Flexible Metal-Organic Framework for Ternary Gas Sieving Separation. *Angew. Chem., Int. Ed.* **2020**, *59*, 22756.
(38) Gücüyener, C.; van den Bergh, J.; Gascon, J.; Kapteijn, F. Ethane/Ethene Separation Turned on Its Head: Selective Ethane Adsorption on the Metal−Organic Framework ZIF-7 through a Gate-Opening Mechanism. *J. Am. Chem. Soc.* **2010**, *132*, 17704−17706.
(39) Li, L.; Lin, R.-B.; Krishna, R.; Li, H.; Xiang, S.; Wu, H.; Li, J.; Zhou, W.; Chen, B. Ethane/ethylene separation in a metal-organic framework with iron-peroxo sites. *Science* **2018**, *362*, 443−446.
(40) Chen, Y.; Wu, H.; Lv, D.; Shi, R.; Chen, Y.; Xia, Q.; Li, Z. Highly Adsorptive Separation of Ethane/Ethylene by An Ethane-Selective MOF MIL-142A. *Ind. Eng. Chem. Res.* **2018**, *57*, 4063−4069.
(41) He, Y.; Zhang, Z.; Xiang, S.; Fronczek, F. R.; Krishna, R.; Chen, B. A Microporous Metal−Organic Framework for Highly Selective Separation of Acetylene, Ethylene, and Ethane from Methane at Room Temperature. *Chem. - Eur. J.* **2012**, *18*, 613−619.
(42) He, Y.; Zhang, Z.; Xiang, S.; Fronczek, F. R.; Krishna, R.; Chen, B. A Robust Doubly Interpenetrated Metal-Organic Framework Constructed from a Novel Aromatic Tricarboxylate for Highly Selective Separation of Small Hydrocarbons. *Chem. Commun.* **2012**, *48*, 6493−6495.
(43) Pei, J.; Wang, J.-X.; Shao, K.; Yang, Y.; Cui, Y.; Wu, H.; Zhou, W.; Li, B.; Qian, G. Engineering Microporous Ethane-Trapping Metal−Organic Frameworks for Boosting Ethane/Ethylene Separation. *J. Mater. Chem. A* **2020**, *8*, 3613−3620.
(44) Chen, Y.; Qiao, Z.; Wu, H.; Lv, D.; Shi, R.; Xia, Q.; Zhou, J.; Li, Z. An Ethane-Trapping MOF PCN-250 for Highly Selective Adsorption of Ethane over Ethylene. *Chem. Eng. Sci.* **2018**, *175*, 110−117.

https://dx.doi.org/10.1021/acsami.0c20000
ACS Appl. Mater. Interfaces 2021, 13, 962−969

Supporting Information

Efficient purification of ethylene from C_2 hydrocarbons with an C_2H_6/C_2H_2-selective metal-organic framework

Shan-Qing Yang,[‡a] Fang-Zhou Sun,[‡a] Puxu Liu,[b] Libo Li,[b] Rajamani Krishna,[c] Ying-Hui Zhang,[a] Quanwen Li,[a] Lei Zhou,[a] and Tong-Liang Hu*[a,d,e]

[a] School of Materials Science and Engineering, Tianjin Key Laboratory of Metal and Molecule-Based Material Chemistry, National Institute for Advanced Materials, Nankai University, Tianjin 300350, China. Email: tlhu@nankai.edu.cn (T.-L. Hu).

[b] College of Chemistry and Chemical Engineering, Shanxi Key Laboratory of Gas Energy Efficient and Clean Utilization, Taiyuan University of Technology, Taiyuan, 030024, Shanxi, China.

[c] Van 't Hoff Institute for Molecular Sciences, University of Amsterdam, Science Park 904, 1098 XH Amsterdam, The Netherlands.

[d] State Key Laboratory of Coordination Chemistry, Nanjing University, Nanjing 210023, China.

[e] Tianjin Key Lab for Rare Earth Materials and Applications, Nankai University, Tianjin 300350, China.

‡ These authors contributed equally to this work.

Experimental Section

Single crystal X-ray diffraction analysis.

The single crystal X-ray diffraction data of **NUM-9** were collected at 293 K, via Rigaku XtaLAB Pro MM007HF DW diffractometer with Cu-Ka radiation (2λ = 1.54184 Å). The structure was solved and refined using Olex2 software with the SHELXT and SHELXL program respectively.[1,2] The crystal details are listed in Table S1, and the crystallographic data of **NUM-9** can be obtained freely from the Cambridge Crystallographic Data Centre (CCDC: 2011498).

Grand Canonical Monte Carlo (GCMC) simulations.

The GCMC simulations were carried out for the adsorption of C_2H_6, C_2H_4 and C_2H_2 in **NUM-9a**. The skeleton of **NUM-9a** and gas molecules were regarded as rigid bodies. The optimal adsorption sites were simulated under 313 K and 1.0 bar by the fixed loading task and Metropolis method. The loading steps, equilibration steps and the production steps were all set to 1.0×10^7. The saturation/maximum uptakes were modeled at 313 K using the fixed pressure task with 0.5×10^7 equilibration steps, followed by 1.0×10^7 production steps for calculating the ensemble averages. The gas–skeleton interaction and the gas–gas interaction were characterized by the standard universal force field (UFF). The atomic partial charges of the host skeleton of **NUM-9a** were used for Qeq method, the guest gas molecules were optimized using the method of DMol3 and adopted the B3LYP fitted charge. The cut-off radius used for the Lennard–Jones interactions is 18.5 Å.[3,4]

Breakthrough simulations.

The performance of industrial fixed bed adsorbers is dictated by a combination of adsorption selectivity and uptake capacity. Transient breakthrough simulations were carried out for 9/90/1 $C_2H_6/C_2H_4/C_2H_2$ mixtures in **NUM-9a** using the methodology described in earlier publications.[5-9] The total pressure in

the fixed bed is 100 kPa. Two different operating temperatures were chosen: 298 K, and 313 K. For the breakthrough simulations, the following parameter values were used: length of packed bed, L = 0.3 m; voidage of packed bed, ε = 0.4; superficial gas velocity at inlet, u = 0.04 m/s.

Nomenclature

L length of packed bed adsorber, m

t time, s

T absolute temperature, K

u superficial gas velocity in packed bed, m s^{-1}

Greek letters

ε voidage of packed bed, dimensionless

τ time, dimensionless

Fitting of pure component isotherms.

The isotherm data for C_2H_6, C_2H_4 and C_2H_2 in **NUM-9a**, measured at 273, 298 and 313 K were fitted with the Dual-site Langmuir-Freundlich model.

$$q = q_{A,sat}\frac{b_A p^{c_A}}{1+b_A p^{c_A}} + q_{B,sat}\frac{b_B p^{c_B}}{1+b_B p^{c_B}}$$

Calculation for C_2H_2/C_2H_4 and C_2H_6/C_2H_4 adsorption selectivities.

The ideal adsorbed solution theory (IAST) was used to estimate the composition of the adsorbed phase from the data of single component isotherms and predict the selectivities of binary mixtures C_2H_2/C_2H_4 and C_2H_6/C_2H_4. IAST calculations of

C_2H_2/C_2H_4 (1/99, 50/50, v/v,) and C_2H_6/C_2H_4 (10/90, 50/50, v/v) mixtures adsorption at 273, 298, 313 K, respectively were performed by

$$S_{ads} = \frac{q_1/q_2}{p_1/p_2}.$$

Table S1. Crystal data and structure refinement parameters for **NUM-9**.

	NUM-9
Formula	$C_{38}H_{36}Mg_2N_2O_{11}$
*M*r (g mol^{-1})	745.31
Crystal system	Orthorhombic
Space group	*Cmca*
a(Å)	26.2428(2)
b(Å)	24.6946(2)
c(Å)	14.0482(2)
α(°)	90
β(°)	90
γ(°)	90
V (Å^3)	9104.01(2)
Z	8
D_c (g cm^{-3})	1.088
F (000)	3120.0
μ (mm^{-1})	0.909
GOF on F^2	0.995
R_1, wR_2 [$I>2\sigma(I)$][a]	0.0686, 0.2093
R_1, wR_2 [all data][b]	0.0736, 0.2150

[a] $R_1 = \sum ||F_o| - |F_c|| / \sum |F_o|$. [b] $wR_2 = \{\sum [w(F_o^2 - F_c^2)^2] / \sum w(F_o^2)^2\}^{1/2}$

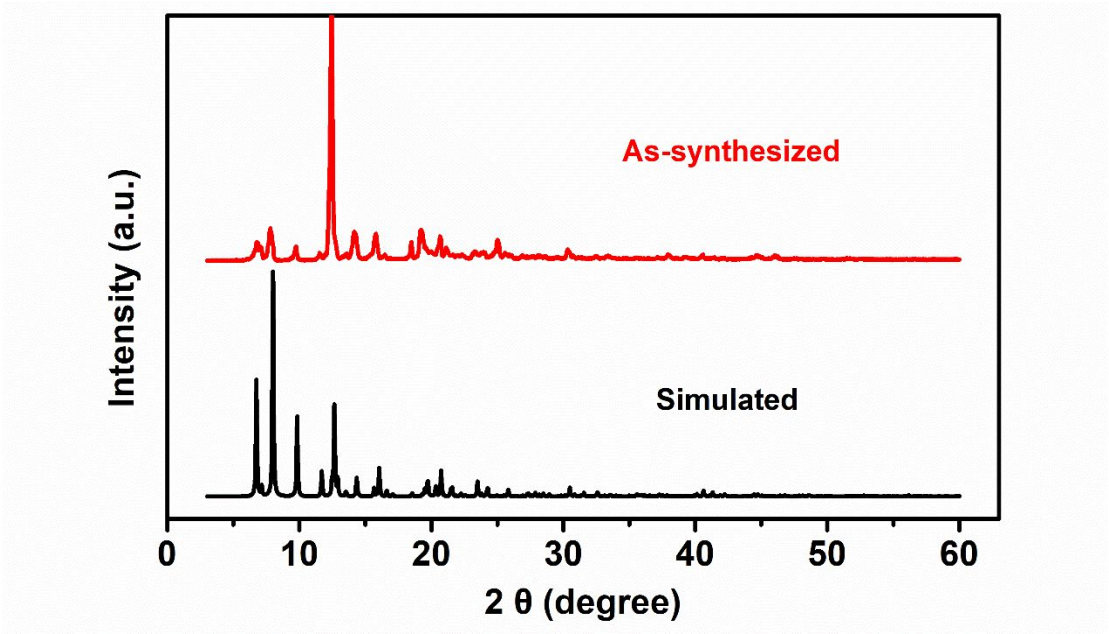

Figure S1. PXRD patterns of **NUM-9**. The experimental result of as-synthesized sample and the simulation from single crystal X-ray diffraction data.

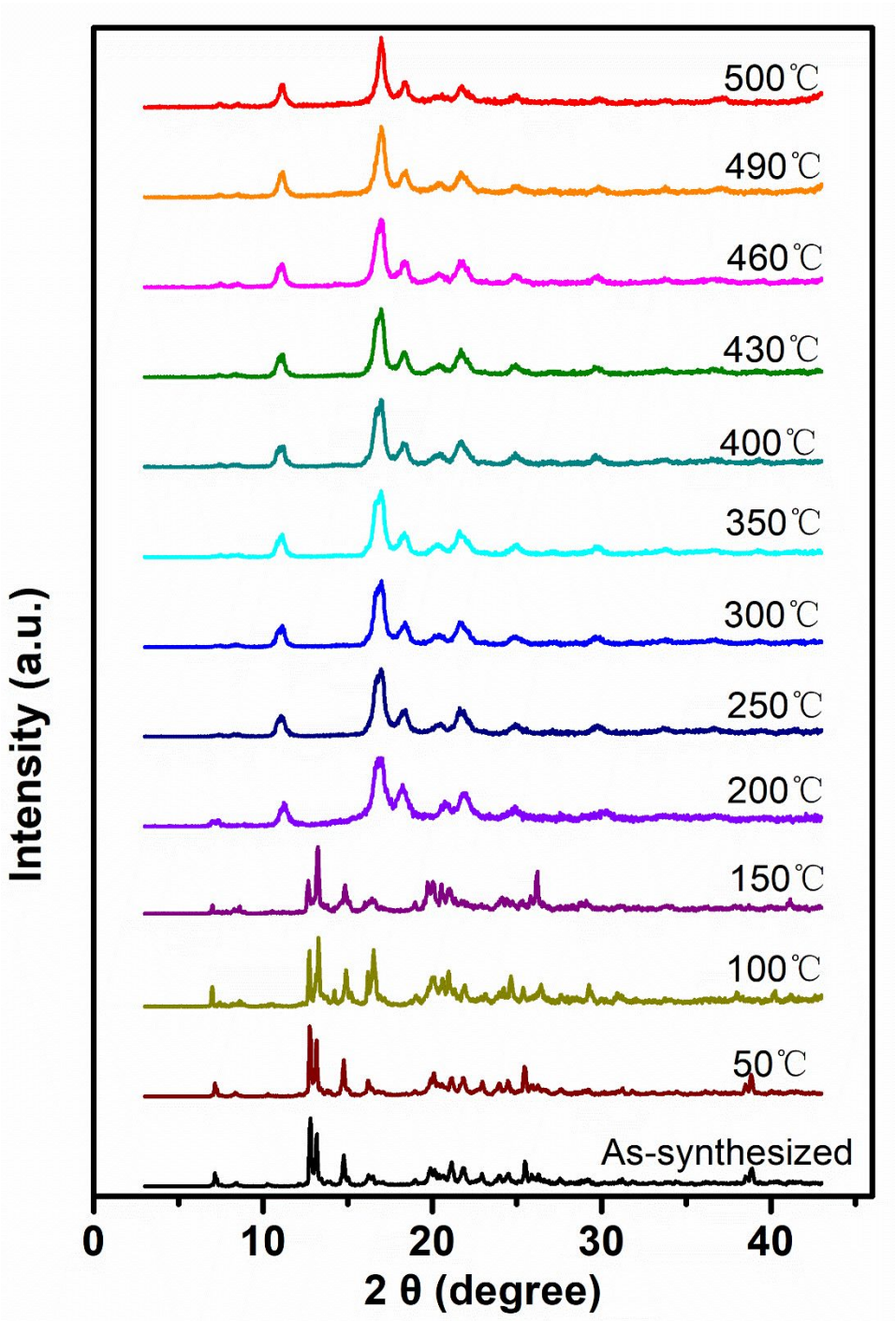

Figure S2. VT-PXRD patterns of **NUM-9** under air atmosphere.

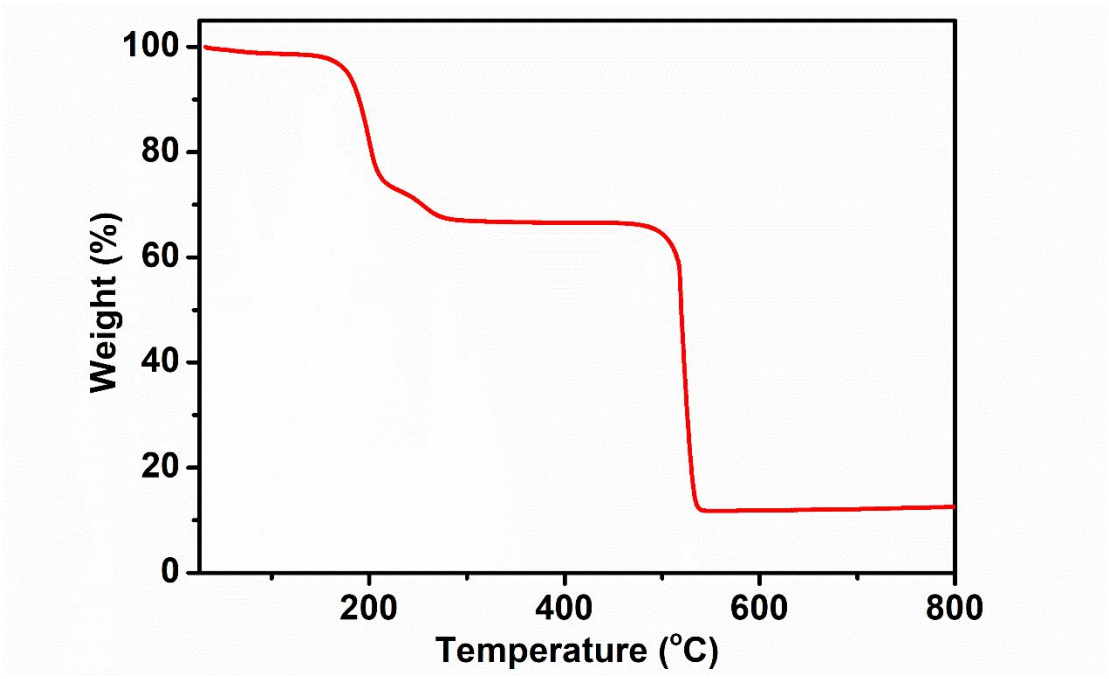

Figure S3. TGA curve for **NUM-9** under air atmosphere.

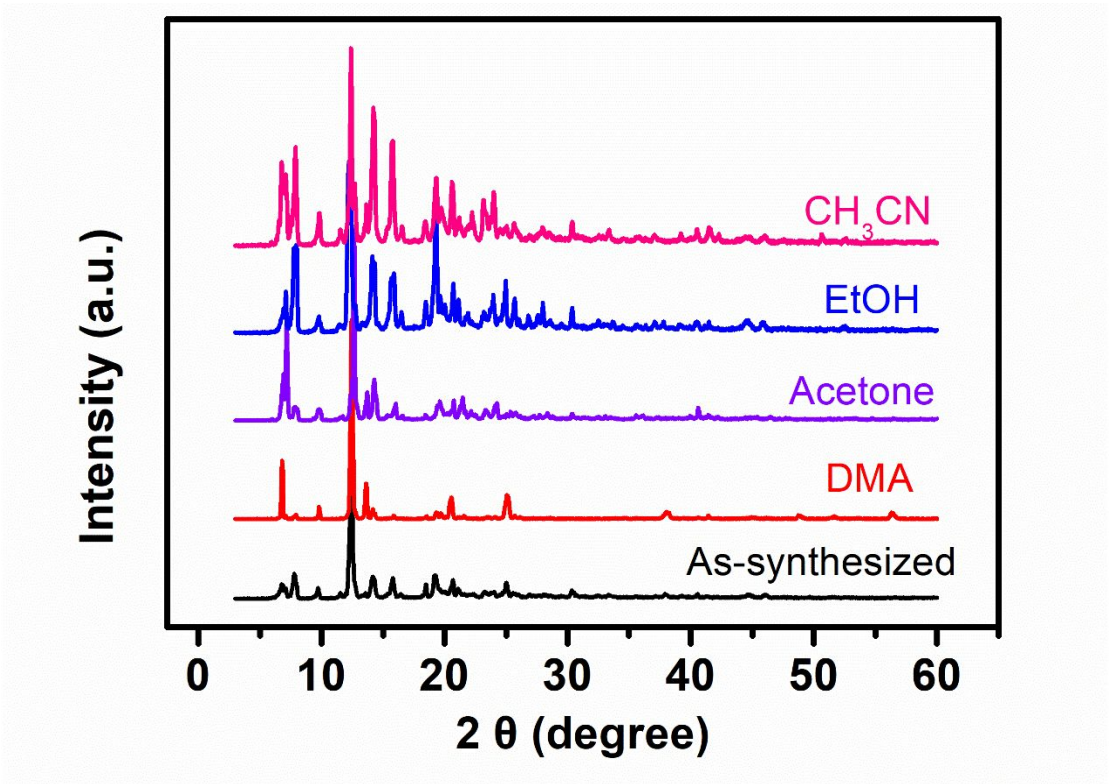

Figure S4. PXRD patterns for **NUM-9** in some solvents for 1 day, showing the structural integrity.

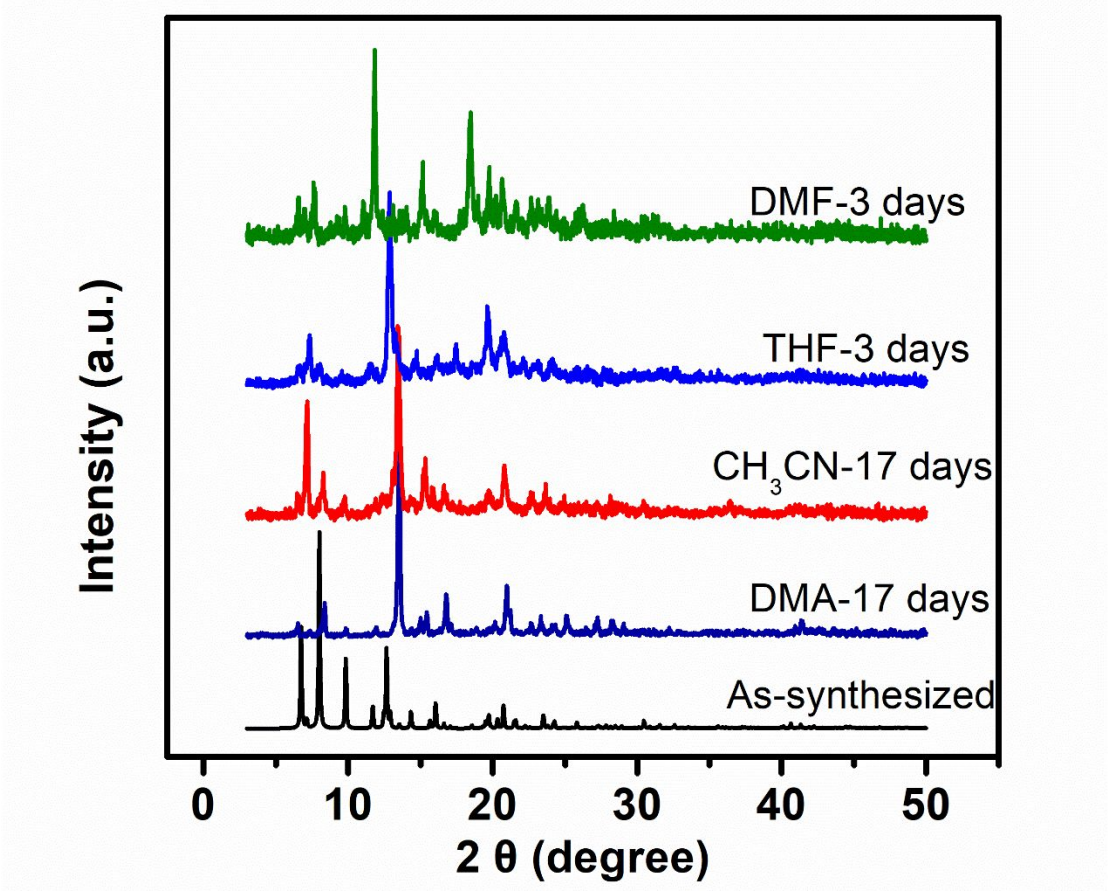

Figure S5. PXRD patterns for **NUM-9** in some solvents for different times showing the structural integrity.

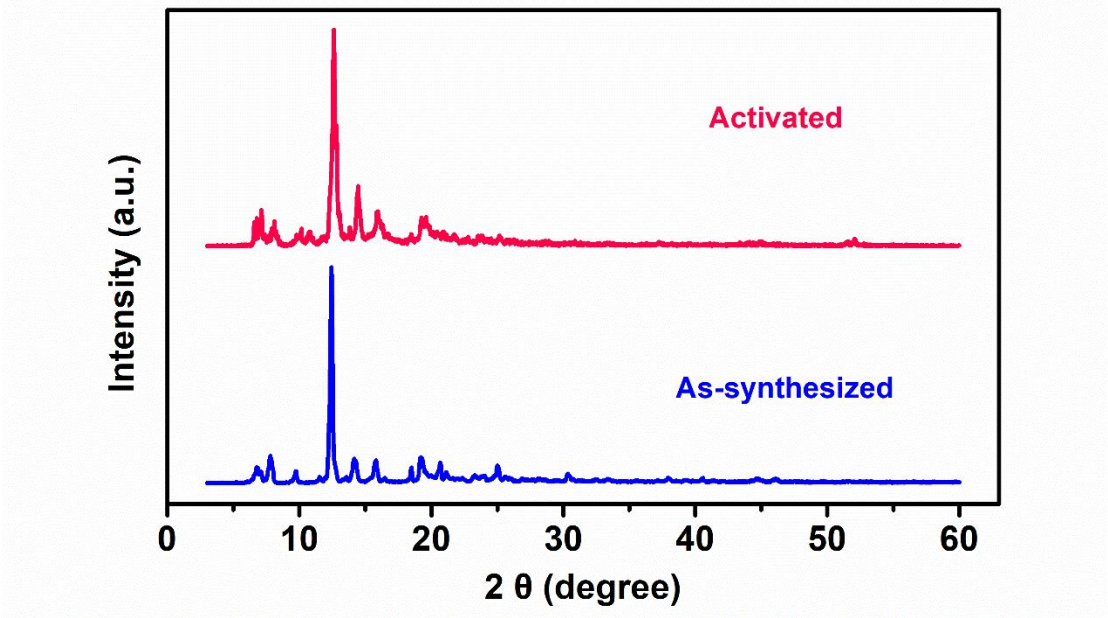

Figure S6. PXRD patterns of **NUM-9** showing that the structure still remains unchanged after activation at 150 °C under vacuum.

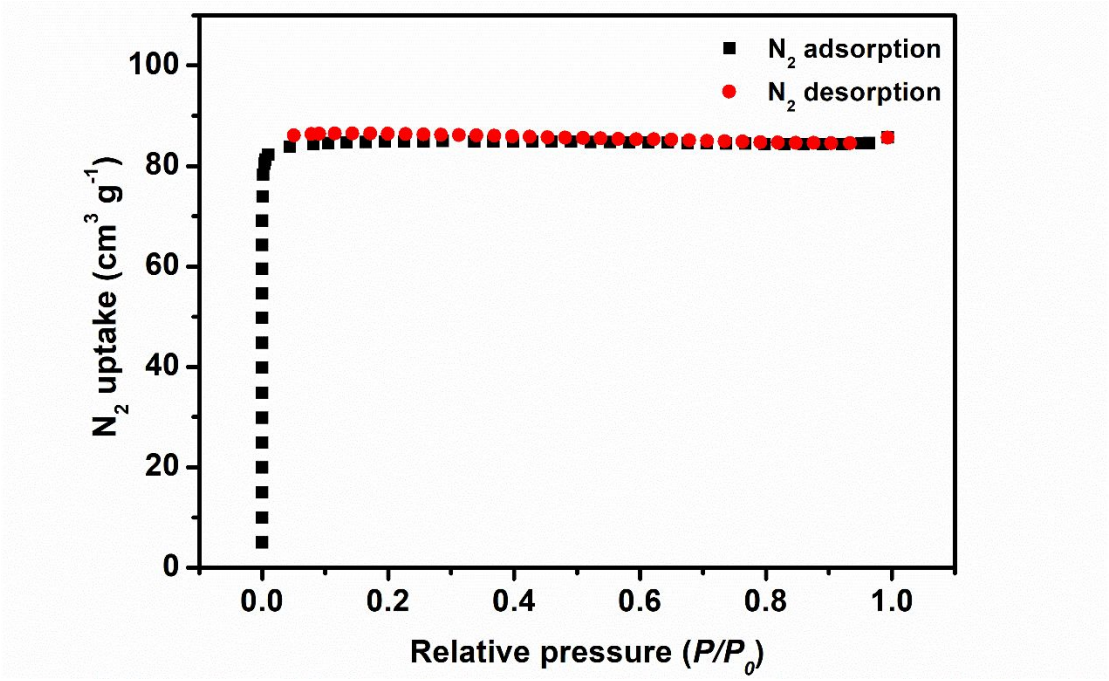

Figure S7. Volumetric N_2 sorption isotherms for **NUM-9a** at 77 K.

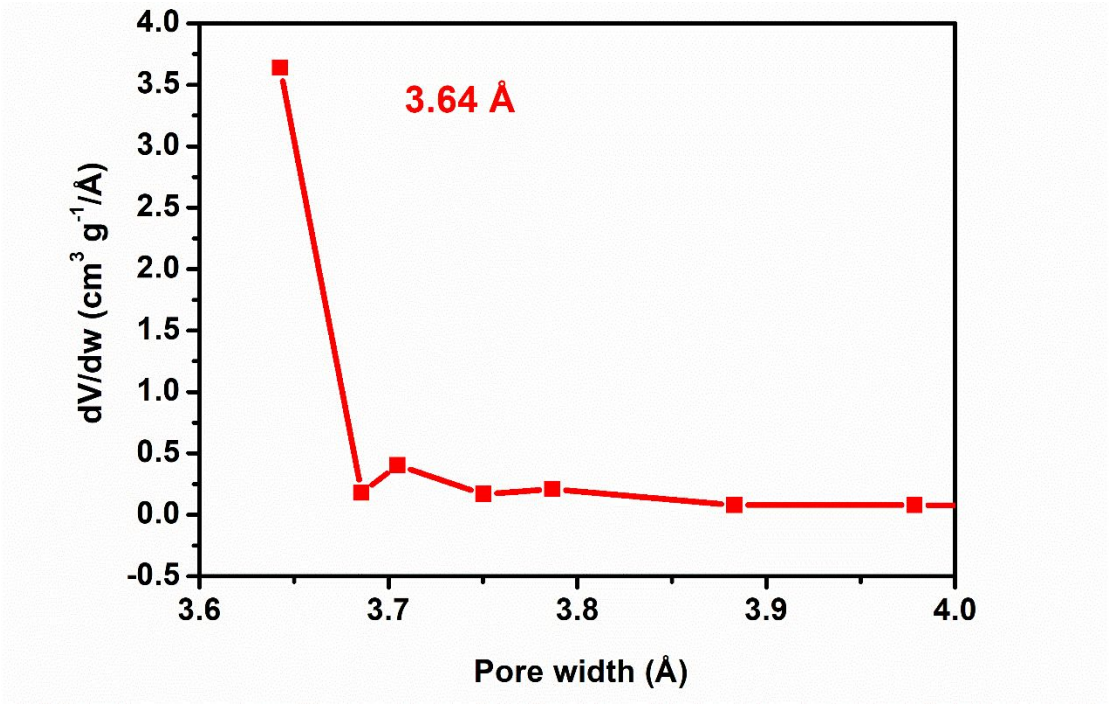

Figure S8. The pore size distribution of **NUM-9a** analyzed using the NLDFT method.

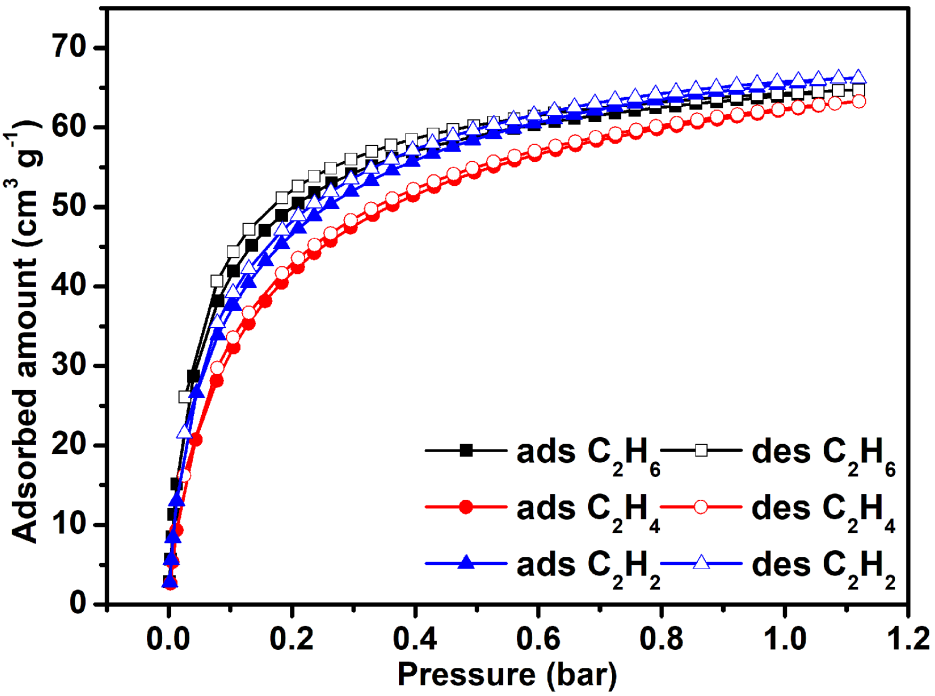

Figure S9. The single-component gas adsorption isotherms for C_2H_6 (dark gray), C_2H_4 (red) and C_2H_2 (blue) of **NUM-9a** at 273 K.

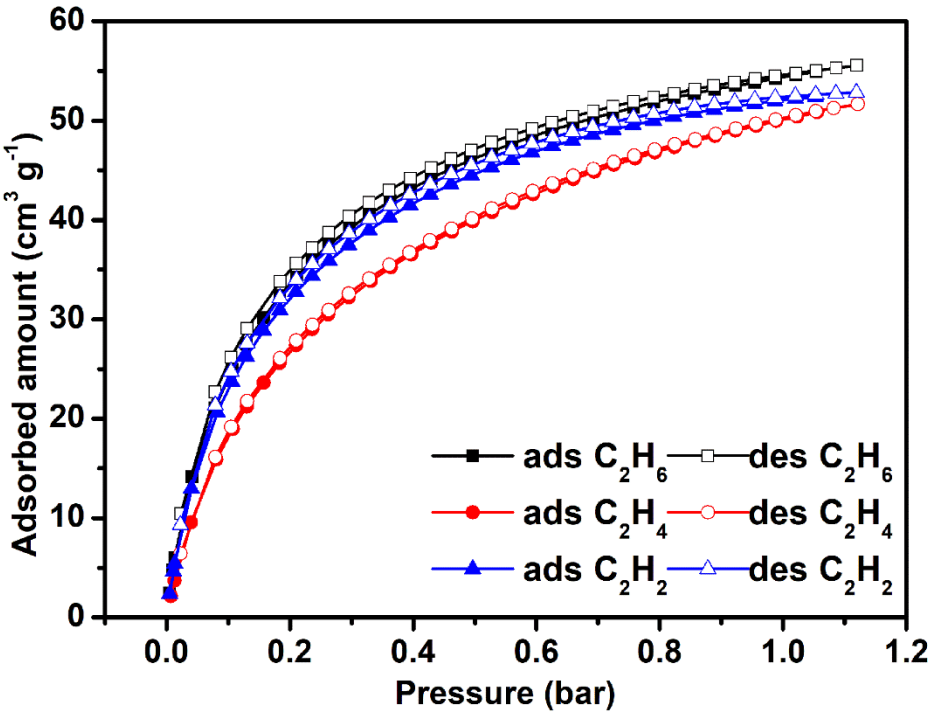

Figure S10. The single-component gas adsorption isotherms for C_2H_6 (dark gray), C_2H_4 (red) and C_2H_2 (blue) of **NUM-9a** at 298 K.

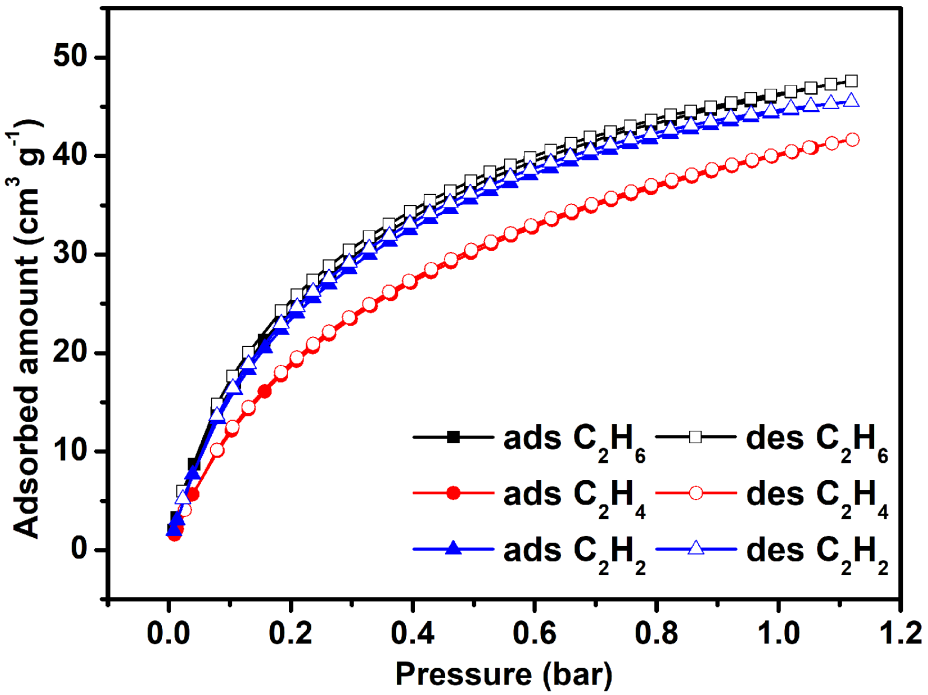

Figure S11. The single-component gas adsorption isotherms for C_2H_6 (dark gray), C_2H_4 (red) and C_2H_2 (blue) of **NUM-9a** at 313 K.

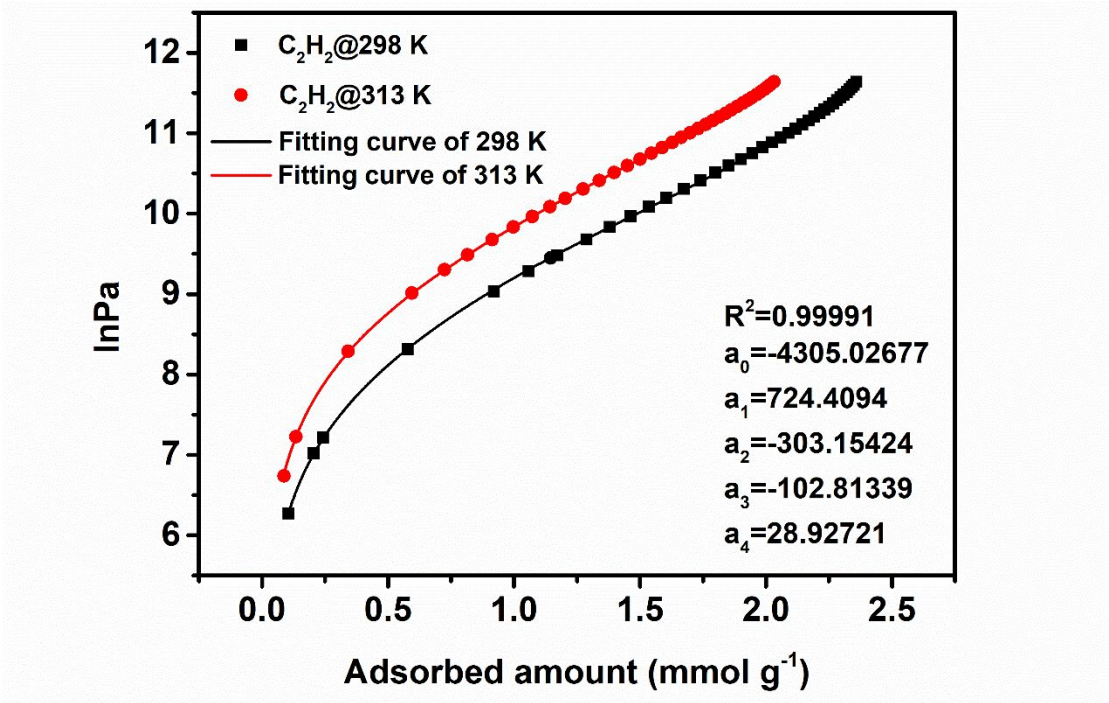

Figure S12. The details of virial equation (solid lines) fitting to the experimental C_2H_2 adsorption data (symbols) for **NUM-9a**.

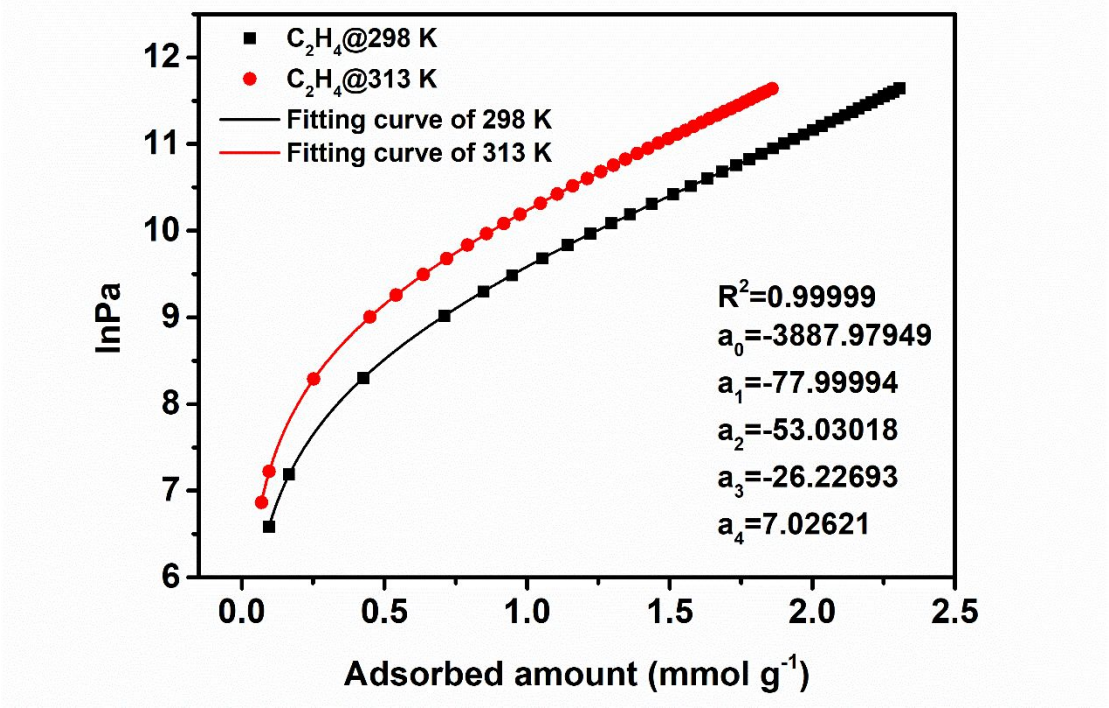

Figure S13. The details of virial equation (solid lines) fitting to the experimental C_2H_4 adsorption data (symbols) for **NUM-9a**.

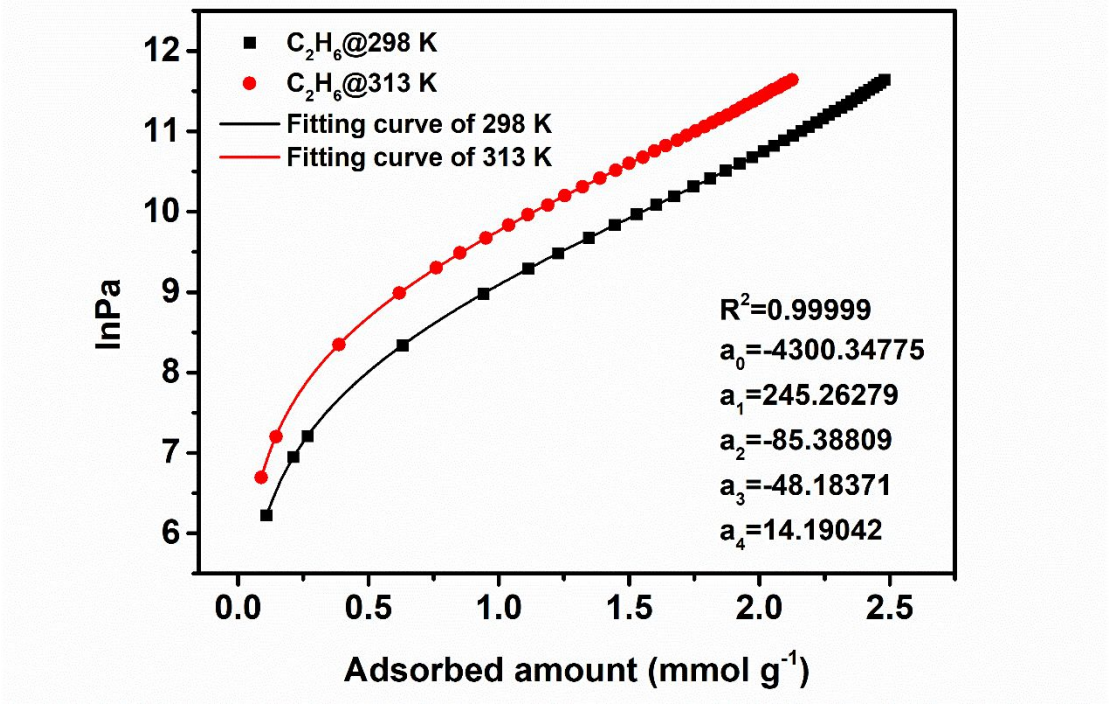

Figure S14. The details of virial equation (solid lines) fitting to the experimental C_2H_6 adsorption data (symbols) for **NUM-9a**.

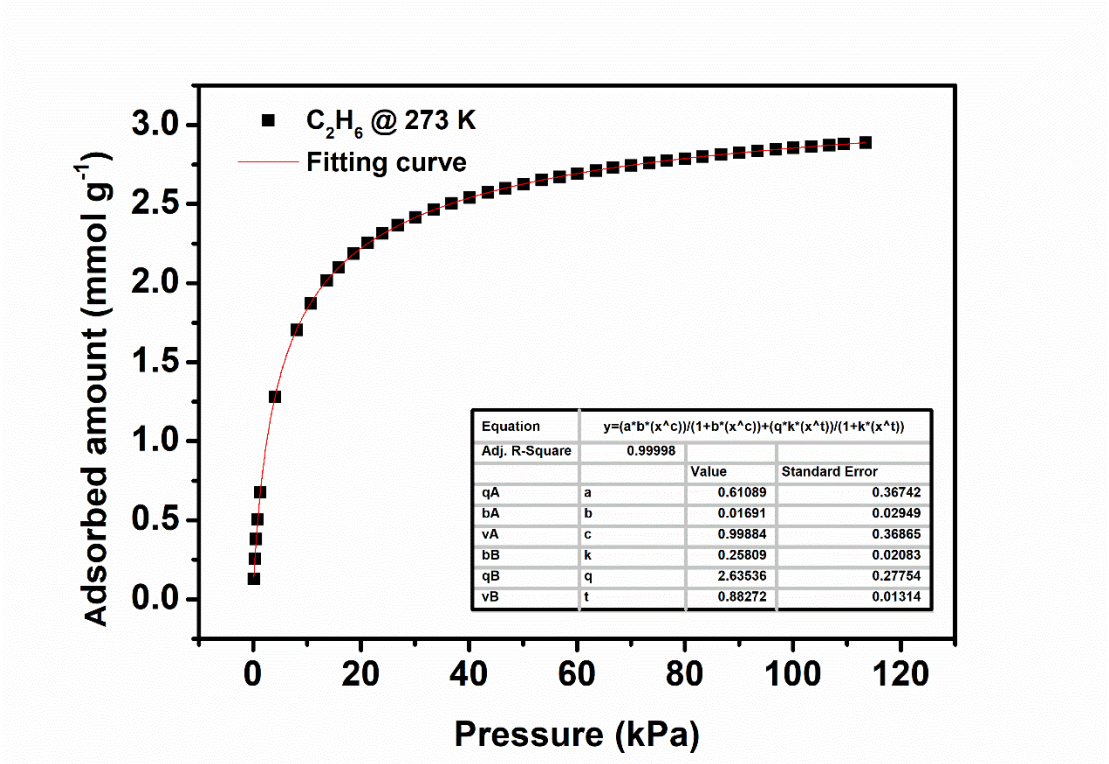

Figure S15. Dual-site Langmuir-Freundlich model for C_2H_6 adsorption isotherm on **NUM-9a** at 273 K.

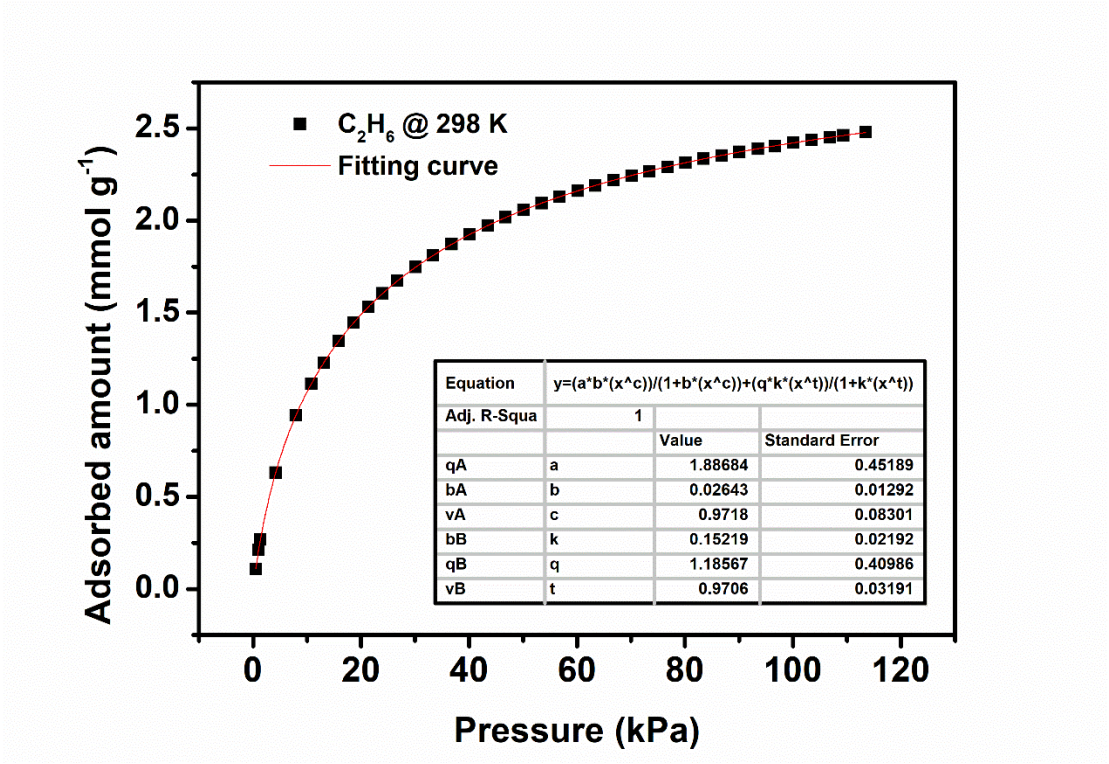

Figure S16. Dual-site Langmuir-Freundlich model for C_2H_6 adsorption isotherm on **NUM-9a** at 298 K.

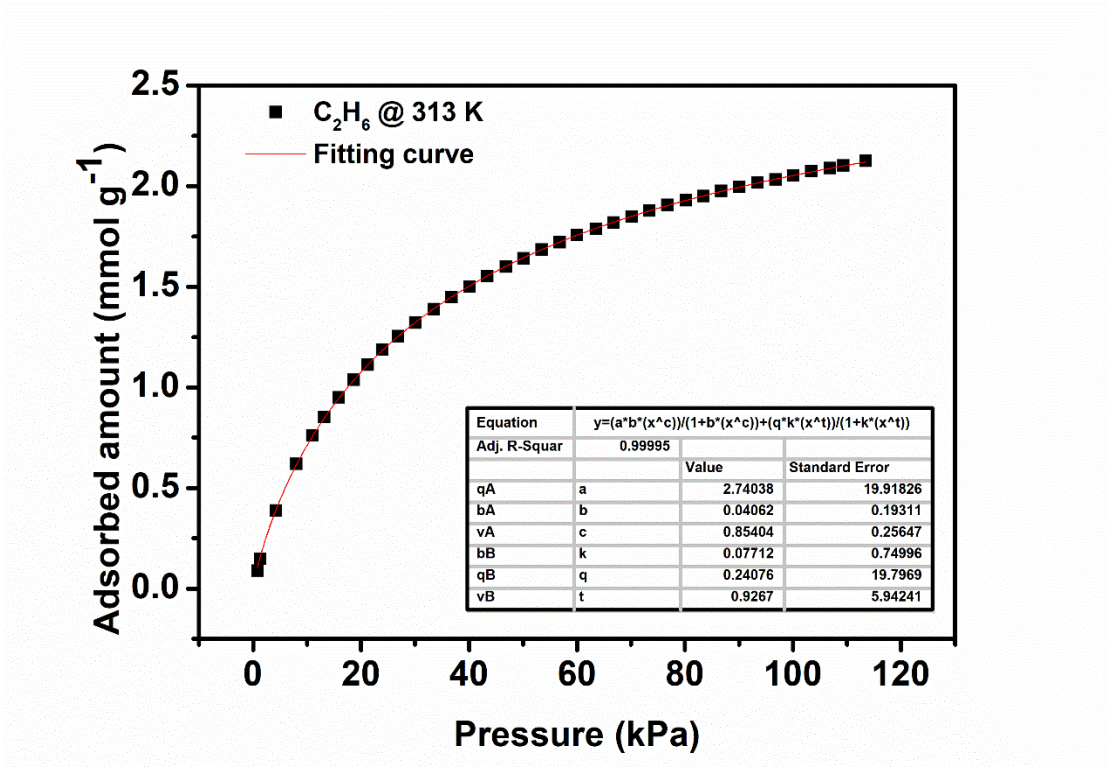

Equation	y=(a*b*(x^c))/(1+b*(x^c))+(q*k*(x^t))/(1+k*(x^t))		
Adj. R-Squar	0.99995		
		Value	Standard Error
qA	a	2.74038	19.91826
bA	b	0.04062	0.19311
vA	c	0.85404	0.25647
bB	k	0.07712	0.74996
qB	q	0.24076	19.7969
vB	t	0.9267	5.94241

Figure S17. Dual-site Langmuir-Freundlich model for C_2H_6 adsorption isotherm on **NUM-9a** at 313 K.

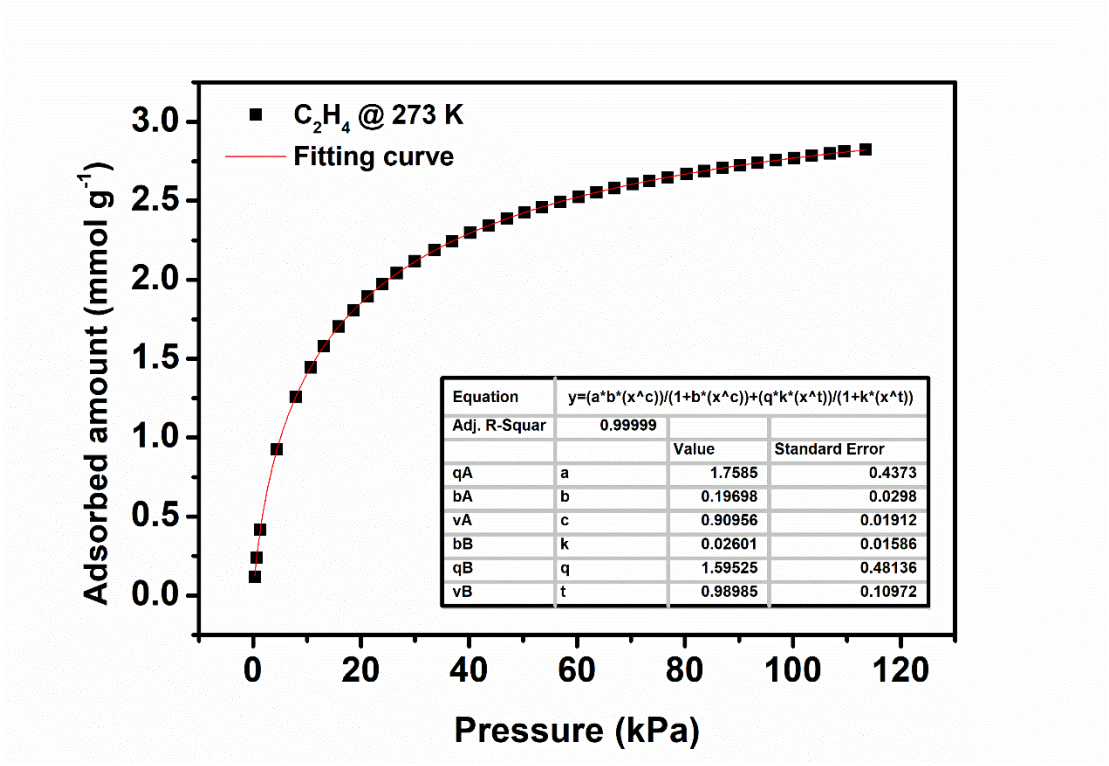

Equation	y=(a*b*(x^c))/(1+b*(x^c))+(q*k*(x^t))/(1+k*(x^t))		
Adj. R-Squar	0.99999		
		Value	Standard Error
qA	a	1.7585	0.4373
bA	b	0.19698	0.0298
vA	c	0.90956	0.01912
bB	k	0.02601	0.01586
qB	q	1.59525	0.48136
vB	t	0.98985	0.10972

Figure S18. Dual-site Langmuir-Freundlich model for C_2H_4 adsorption isotherm on **NUM-9a** at 273 K.

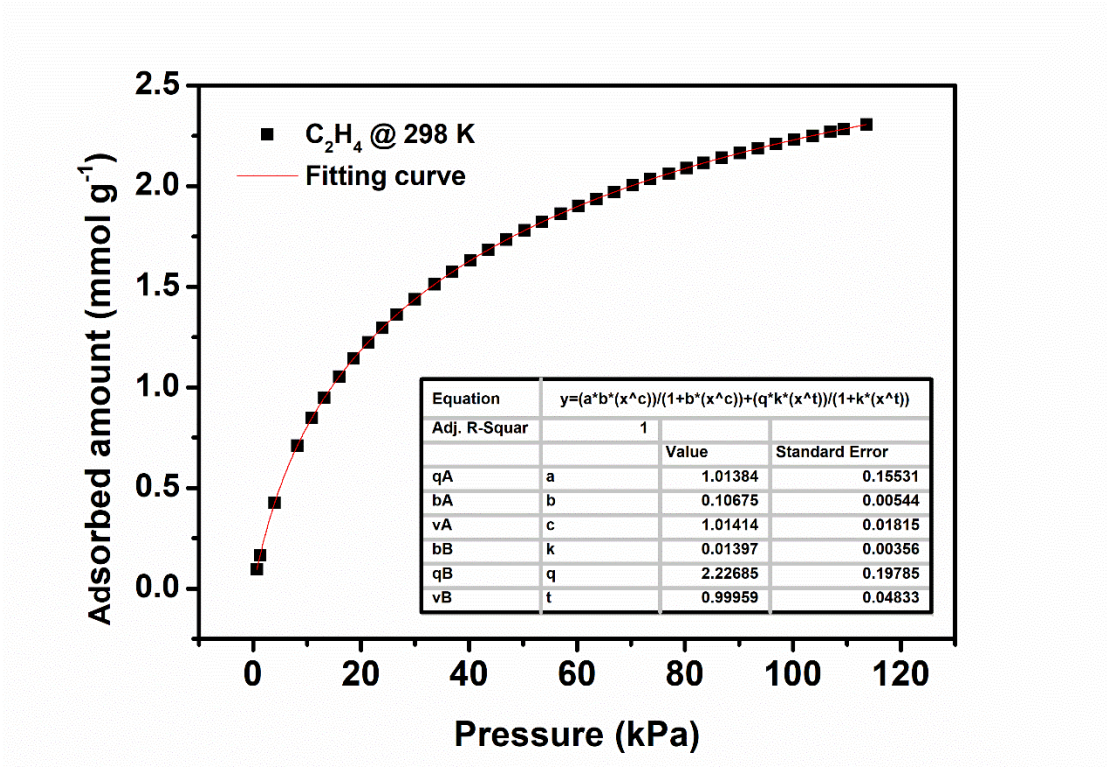

Figure S19. Dual-site Langmuir-Freundlich model for C_2H_4 adsorption isotherm on **NUM-9a** at 298 K.

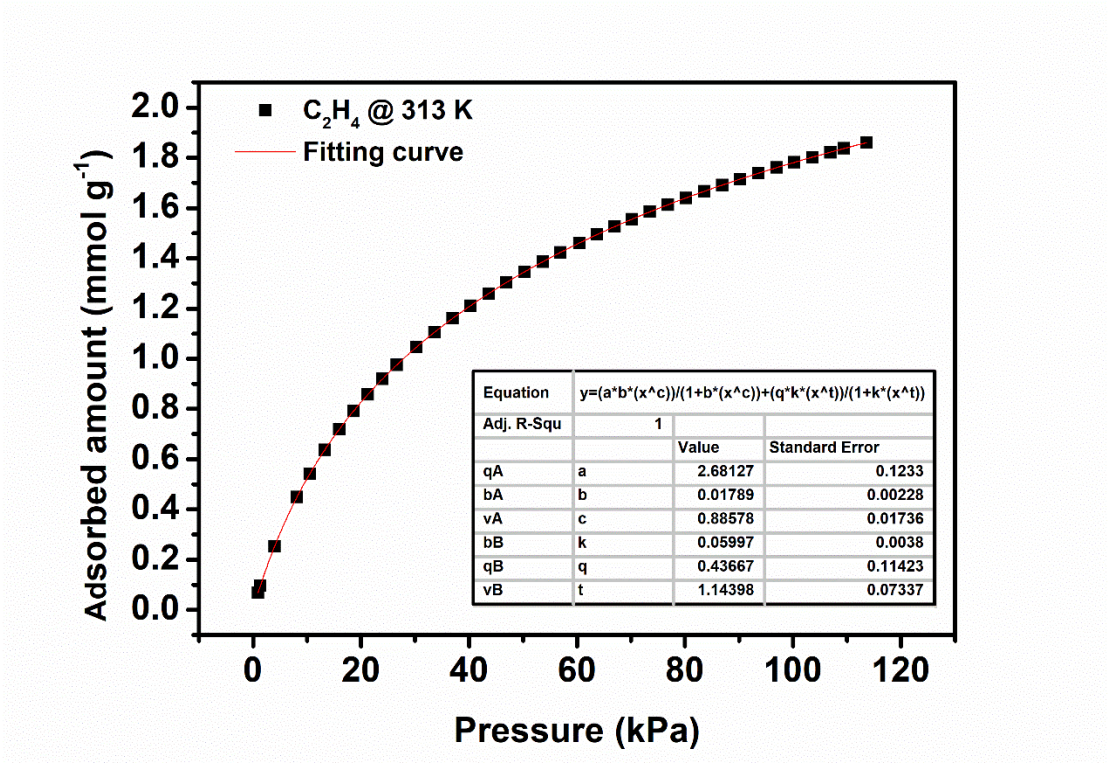

Figure S20. Dual-site Langmuir-Freundlich model for C_2H_4 adsorption isotherm on **NUM-9a** at 313 K.

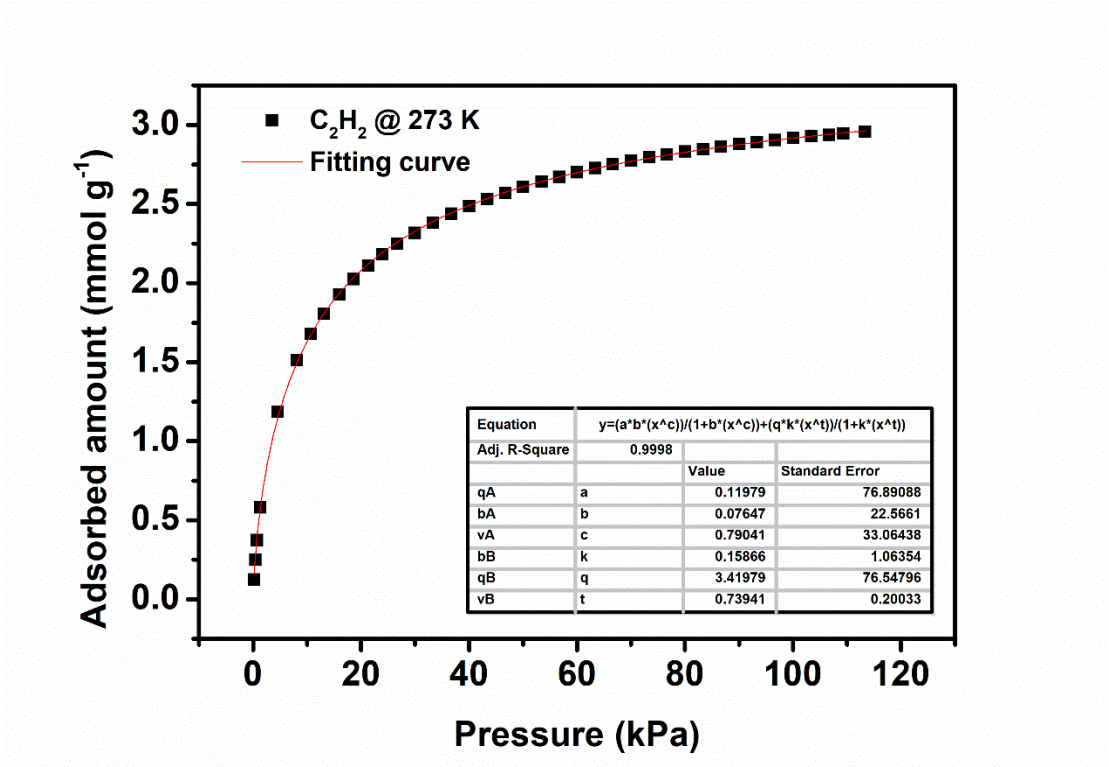

Figure S21. Dual-site Langmuir-Freundlich model for C_2H_2 adsorption isotherm on **NUM-9a** at 273 K.

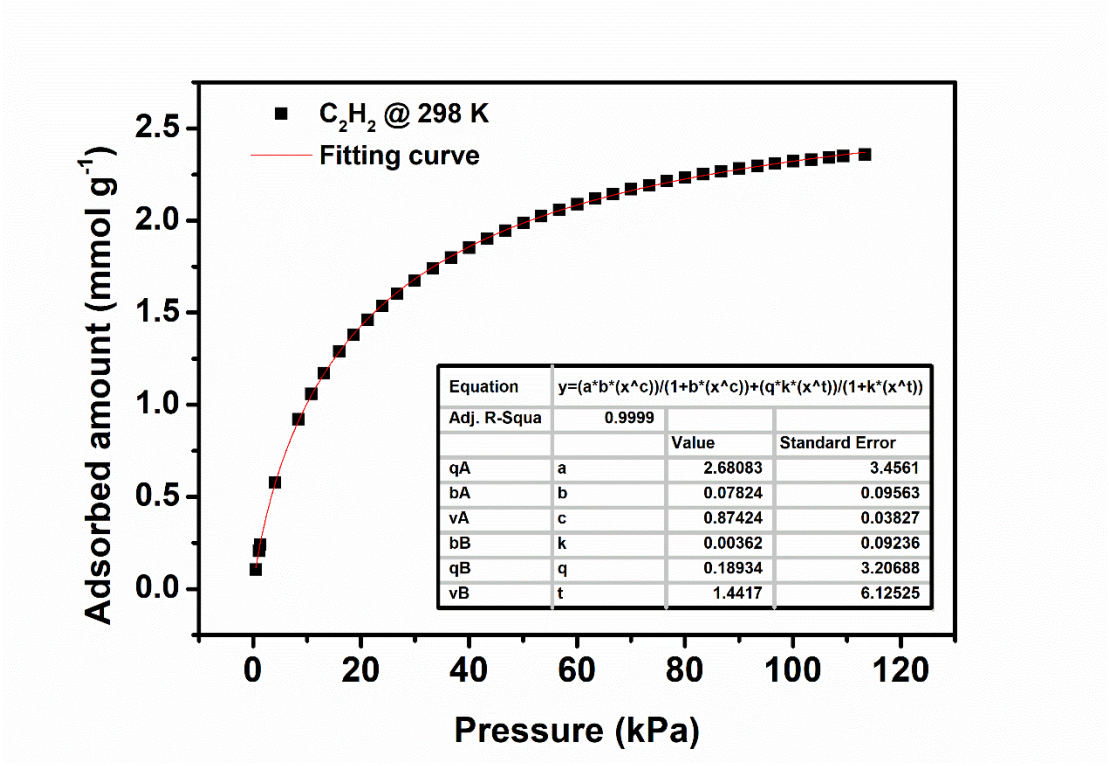

Figure S22. Dual-site Langmuir-Freundlich model for C_2H_2 adsorption isotherm on **NUM-9a** at 298 K.

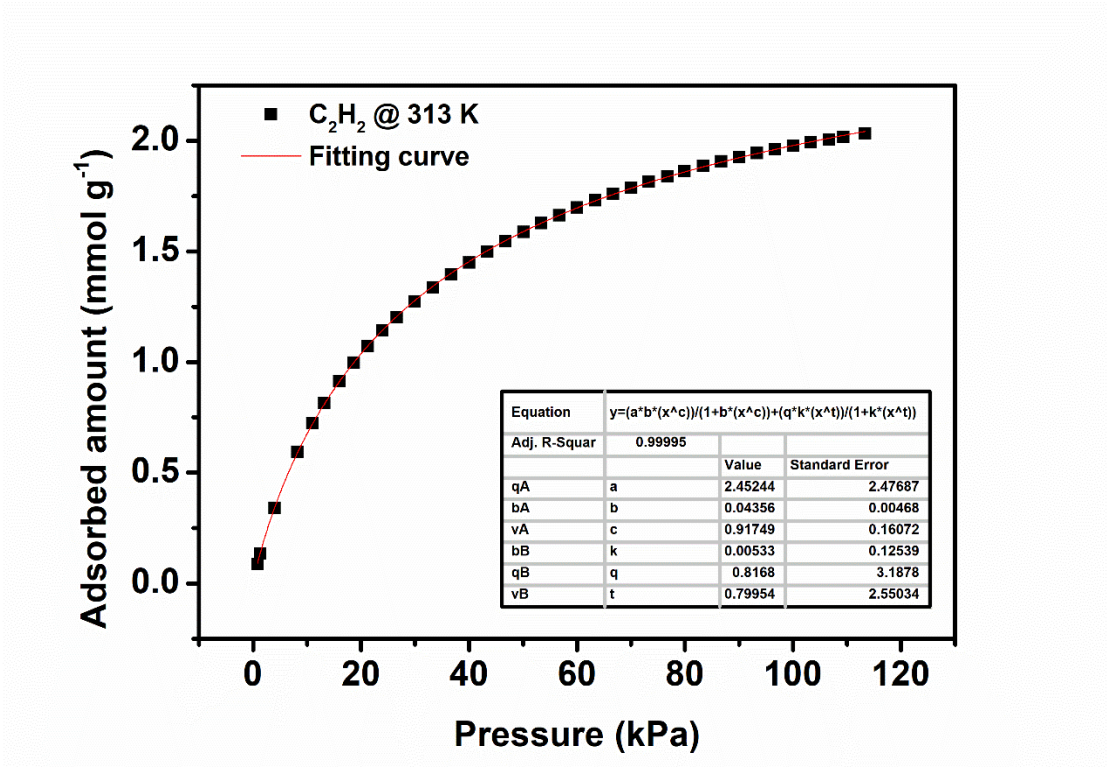

Equation	y=(a*b*(x^c))/(1+b*(x^c))+(q*k*(x^t))/(1+k*(x^t))		
Adj. R-Squar	0.99995		
		Value	Standard Error
qA	a	2.45244	2.47687
bA	b	0.04356	0.00468
vA	c	0.91749	0.16072
bB	k	0.00533	0.12539
qB	q	0.8168	3.1878
vB	t	0.79954	2.55034

Figure S23. Dual-site Langmuir-Freundlich model for C_2H_2 adsorption isotherm on **NUM-9a** at 313 K.

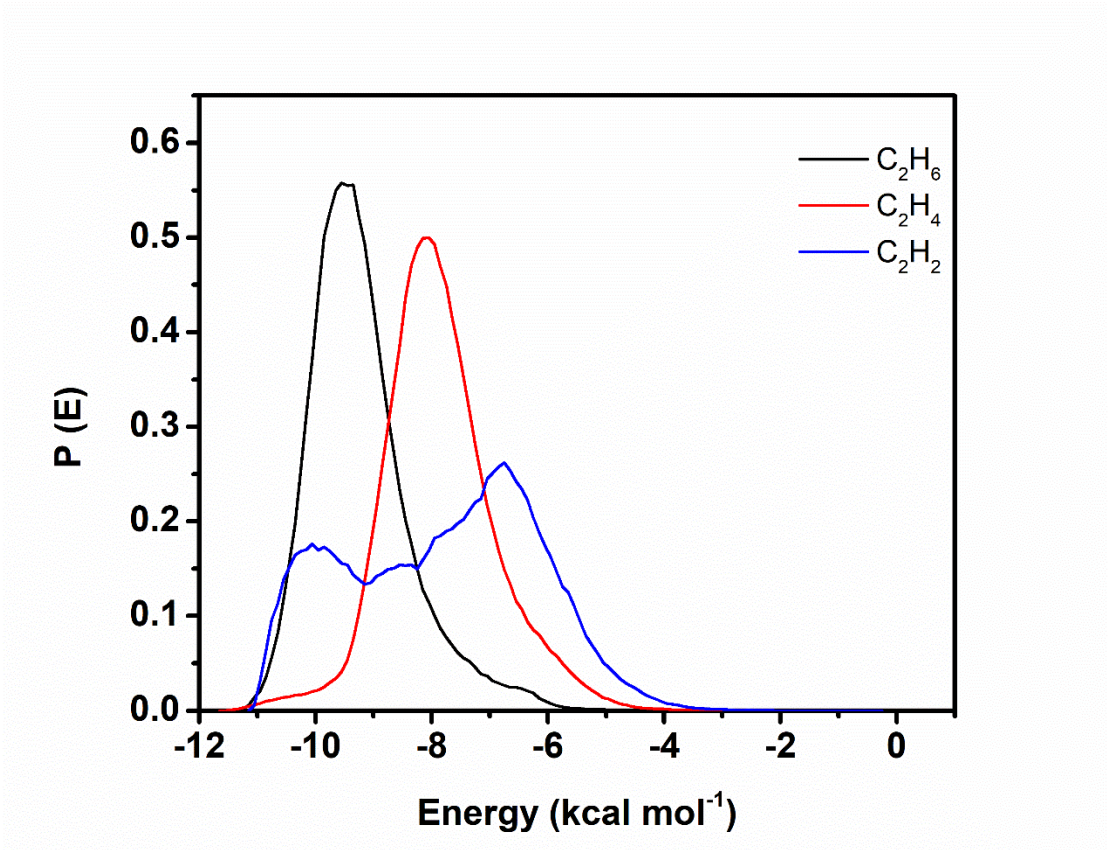

Figure S24. Energy distribution of C_2H_6, C_2H_4 and C_2H_2 during adsorption in **NUM-9a**.

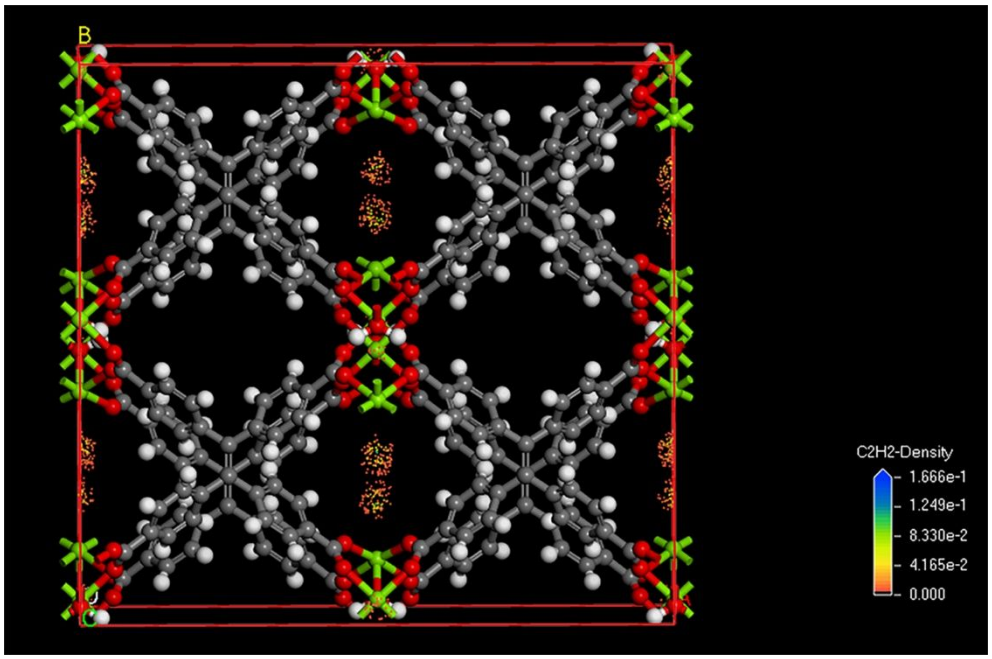

Figure S25. Density distribution of C_2H_2 in **NUM-9a**.

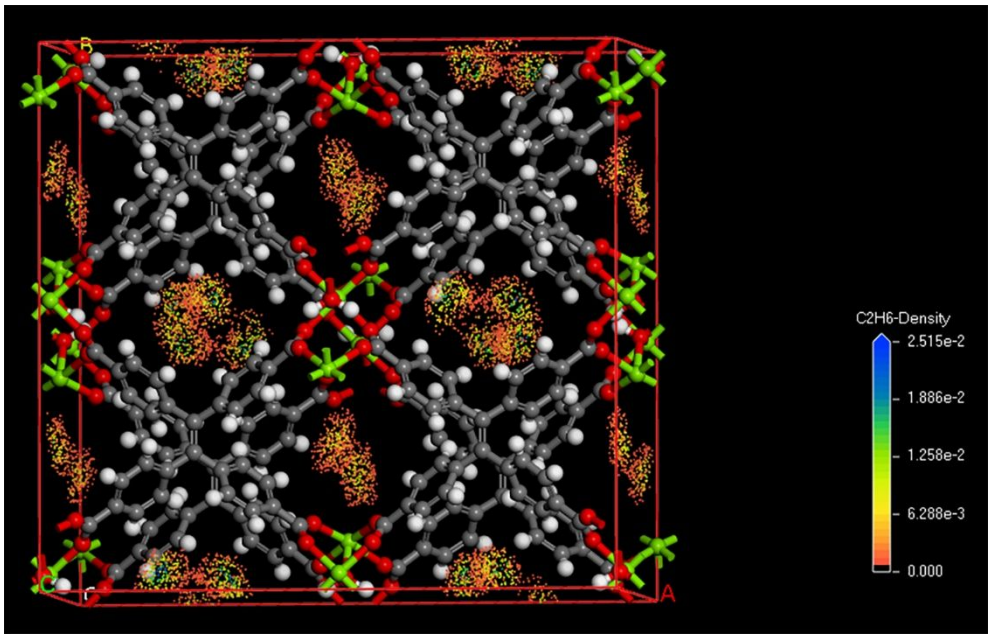

Figure S26. Density distribution of C_2H_6 in **NUM-9a**.

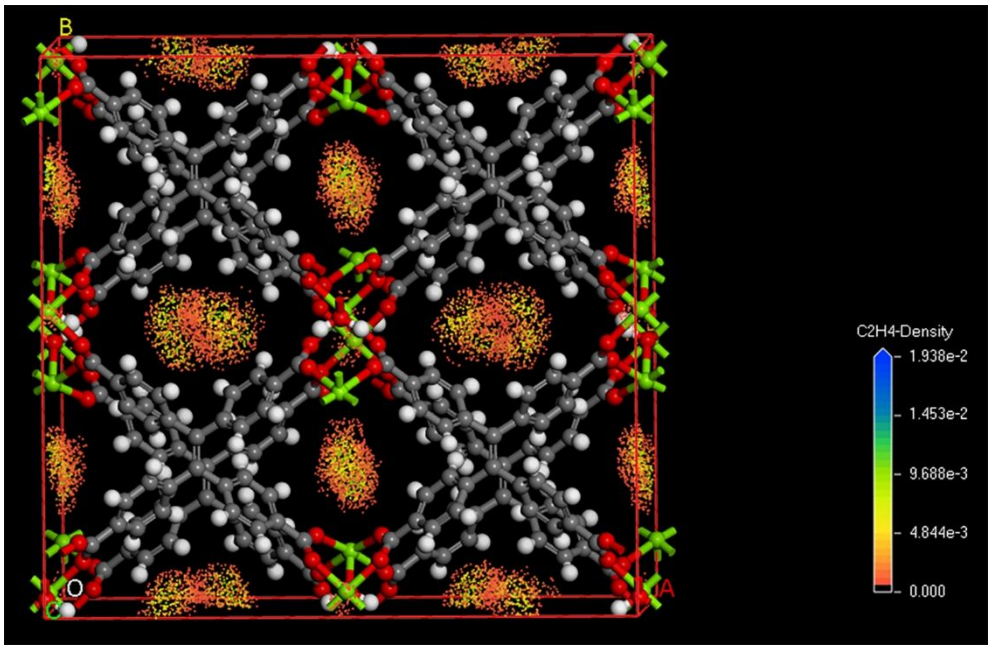

Figure S27. Density distribution of C_2H_4 in **NUM-9a**.

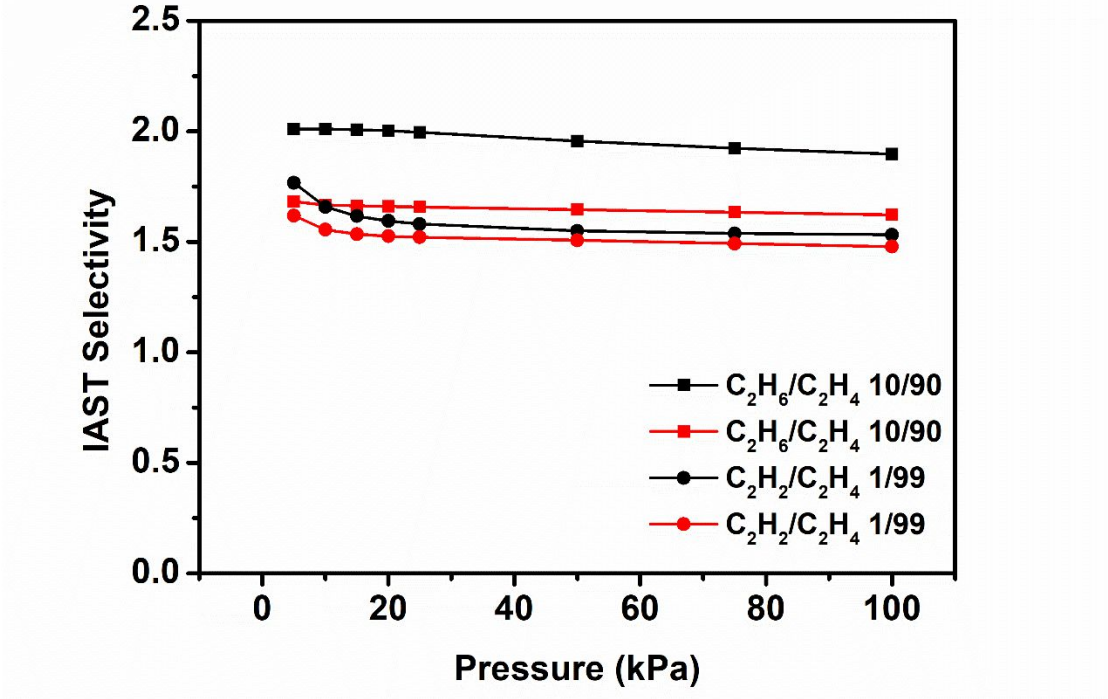

Figure S28. IAST selectivities of mixture of C_2H_6/C_2H_4 (10/90, v/v) and C_2H_2/C_2H_4 (1/99, v/v) for **NUM-9a** at 273 (black) and 298 (red) K.

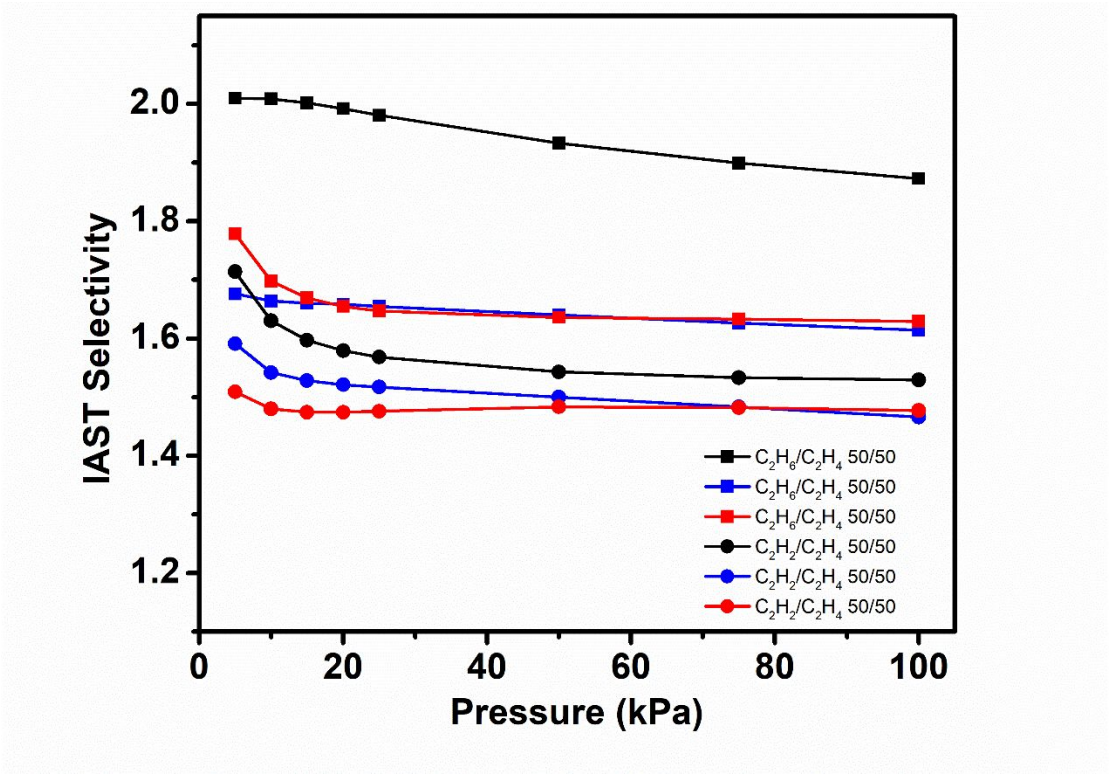

Figure S29. IAST selectivities of mixture of C_2H_6/C_2H_4 (50/50, v/v) and C_2H_2/C_2H_4 (50/50, v/v) for **NUM-9a** at 273 (black), 298 (blue) K and 313 (red) K.

Reference

[1]. Dolomanov, O. V.; Bourhis, L. J.; Gildea, R. J.; Howard, J. A. K.; Puschmann, H. *J. Appl. Crystallogr.*, **2009**, 42, 339-341.

[2]. Hanfland, M. *Acta Crystallogr., Sect. A*, **2015**, 71, s3.

[3]. Zhou, D. D.; He, C. T.; Liao, P. Q.; Xue, W.; Zhang, W. X.; Zhou, H. L.; Zhang, J. P.; Chen, X. M. *Chem. Commun.,* **2013**, 49, 11728-11730.

[4]. Wu, Y.; Chen, H.; Liu, D.; Qian, Y.; Xi, H. *Chem. Eng. Sci.*, **2015**, 124, 144-153.

[5]. Krishna, R. *Micropor. Mesopor. Mater.*, **2014**, 185, 30-50.

[6]. Krishna, R. *RSC Adv.*, **2015**, 5, 52269-52295.

[7]. Krishna, R. *RSC Adv.*, **2017**, 7, 35724-35737.

[8]. Krishna, R. *Sep. Purif. Technol.*, **2018**, 194, 281-300.

[9]. Krishna, R. *ACS Omega*, **2020**, 5, 16987-17004.